

# Constraining $\Lambda$ CDM cosmological parameters with Einstein Telescope mock data

Matteo Califano,<sup>1,2\*</sup> Ivan de Martino,<sup>3†</sup> Daniele Vernieri<sup>4,1,2‡</sup> and Salvatore Capozziello<sup>4,1,2§</sup>

<sup>1</sup>*Scuola Superiore Meridionale, Largo San Marcellino 10, I-80138, Naples, Italy*

<sup>2</sup>*INFN Sezione di Napoli, Compl. Univ. di Monte S. Angelo, Edificio G, Via Cinthia, I-80126, Napoli, Italy*

<sup>3</sup>*Universidad de Salamanca, Departamento de Física Fundamental, P. de la Merced S/N, Salamanca, ES*

<sup>4</sup>*Dipartimento di Fisica, Università di Napoli “Federico II”, Compl. Univ. di Monte S. Angelo, Edificio G, Via Cinthia, I-80126, Napoli, Italy*

Accepted XXX. Received YYY; in original form ZZZ

## ABSTRACT

We investigate the capability of Einstein Telescope to constrain the cosmological parameters of the non-flat  $\Lambda$ CDM cosmological model. Two types of mock datasets are considered depending on whether or not a short Gamma-Ray Burst is detected and associated with the gravitational wave emitted by binary neutron stars merger using the THESEUS satellite. Depending on the mock dataset, two statistical estimators are applied: one assumes that the redshift is known, while the other marginalizes over it assuming a specific redshift prior distribution. We demonstrate that (i) using mock catalogs collecting gravitational wave signals emitted by binary neutron stars systems to which a short Gamma-Ray Burst has been associated, Einstein Telescope may achieve an accuracy on the cosmological parameters of  $\sigma_{H_0} \approx 0.40 \text{ km s}^{-1} \text{ Mpc}^{-1}$ ,  $\sigma_{\Omega_{k,0}} \approx 0.09$ , and  $\sigma_{\Omega_{\Lambda,0}} \approx 0.07$ ; while (ii) using mock catalogs collecting all gravitational wave signals emitted by binary neutron stars systems for which an electromagnetic counterpart has not been detected, Einstein Telescope may achieve an accuracy on the cosmological parameters of  $\sigma_{H_0} \approx 0.04 \text{ km s}^{-1} \text{ Mpc}^{-1}$ ,  $\sigma_{\Omega_{k,0}} \approx 0.01$ , and  $\sigma_{\Omega_{\Lambda,0}} \approx 0.01$ , once the redshift probability distribution of GW events is known from population synthesis simulations and/or the measure of the tidal deformability parameter. These results show an improvement of a factor 2–75 with respect to earlier results using complementary datasets.

**Key words:** cosmological parameters, gravitational waves, neutron star mergers, gamma ray bursts, cosmology: observations

ET preprint code: ET-0111A-22

## 1 INTRODUCTION

The concordance cosmological model, known as  $\Lambda$  Cold Dark Matter ( $\Lambda$ CDM), fits remarkably well most of the current cosmological and astrophysical observations. For instance, the *Planck* satellite measured with unprecedented precision the Cosmic Microwave Background (CMB) temperature anisotropies providing the most powerful tool to constrain the cosmological parameters. It favours a Universe whose accelerated expansion is determined by a cosmological constant, and whose self-gravitating structures form consequently to the gravitational collapse of baryonic matter in the potential well of the dark matter haloes (Planck Collaboration et al. 2020a,b). However, without a doubt, the three fundamental pillars of the  $\Lambda$ CDM model, namely inflation, dark matter, and dark energy have yet to be thoroughly tested and understood. In particular, dark matter and dark

energy are necessary to obtain a good fit of cosmological and astrophysical data but their fundamental nature, *i.e.* whether they are particles or fields, is still a puzzle (Capozziello & De Laurentis 2012; de Martino et al. 2020; Salucci et al. 2021).

While we ignore their fundamental nature, some tensions in the  $\Lambda$ CDM model begin to appear as precision in observations improves (Verde et al. 2019; Abdalla et al. 2022). The best known is the Hubble tension (Vagnozzi 2020; Di Valentino et al. 2021a), that is the discrepancy in the estimates of the Hubble constant obtained by local and early measurements (Philcox et al. 2020; Wong et al. 2020; Riess et al. 2021a; Dainotti et al. 2021, 2022; Philcox et al. 2022). This tension reaches the statistical level of  $4.2 \sigma$  difference and it is one of the most debated tensions in cosmology. Early measurements rely on fitting the CMB power spectra in the framework of the  $\Lambda$ CDM model. Using Planck data, one obtains a Hubble constant equal to  $H_0 = 67.27 \pm 0.60 \text{ km s}^{-1} \text{ Mpc}^{-1}$  at 68% of confidence level (Planck Collaboration et al. 2020b). On the other hand, late measurements rely on *standard candles*, which must be calibrated to build the so-called *cosmic distance ladder*. Indeed, geometrical measurements of the distance obtained from the parallax are used to calibrate the luminosities of the so-called *standard candles*. These are astrophysical objects, such as pulsating Cepheid variables and

\* E-mail: matteo.califano@unina.it

† E-mail: ivan.demartino@usal.es, Corresponding author

‡ E-mail: danielle.vernieri@unina.it

§ E-mail: capozziello@unina.it

Type Ia supernovae (SNIa), which show a tight correlation between the intrinsic luminosity and some observational quantities. Using 75 Milky Way Cepheids from the third data release of the Gaia mission, the local measurement of the Hubble constant results to be  $H_0 = 73.2 \pm 1.3 \text{ km s}^{-1} \text{ Mpc}^{-1}$  at 68% of confidence level (Riess et al. 2021b). This represents a  $4.2\sigma$  with the CMB data. Although many explanations have been provided (Di Valentino et al. 2021a; Capozziello et al. 2020), the debate on the origin of this tension is still open.

Anyway, the Hubble tension is not the only one, there are others such as the so-called  $S_8$  tension between Planck data and the weak lensing measurements, and the statistical preference of a closed Universe (Di Valentino et al. 2020; Handley 2021; Di Valentino et al. 2021b; Nunes & Vagnozzi 2021; Vagnozzi et al. 2021; Luongo & Muccino 2022). The latter appears to resolve the tension between the estimation and the expectation value of the lensing amplitude obtained from the CMB power spectra (Di Valentino et al. 2020). Nevertheless, a non-flat  $\Lambda$ CDM model is far from being confirmed. Indeed, the CMB temperature and polarization spectra are shown to be consistent with a spatially flat Universe (Efstathiou & Gratton 2020; Park & Ratra 2020). Additionally, a recent analysis of the cosmic shear from the Kilo-Degree Survey does not find any statistical evidence in favour of a closed Universe (Tröster et al. 2021).

One way to solve these tensions lies in estimating the Hubble constant and the curvature parameter with observations complementary to the standard candles or to the CMB power spectrum. This possibility relies on the Gravitational Waves (GWs) that allow us to estimate the distance of the source (Schutz 1986; Capozziello et al. 2010). GWs from a binary black hole merger were first detected in 2015 (Abbott et al. 2016a). Right from the onset, GW astronomy has generated novel ways to test fundamental physics: clear examples are the tests of gravity in the strong-field regime (Abbott et al. 2016a,b), and the first high-precision measurement of the GW speed (Abbott et al. 2017a) which spectacularly ruled out large classes of gravitational theories (Ezquiaga & Zumalacárregui 2017). The opportunities to test the dark Universe will multiply as GW data continues to improve and new experiments come online, *e.g.* Einstein Telescope (ET) (Maggiore et al. 2020). Nevertheless, GWs are not free of issues. The luminosity distance can be determined from the waveform, otherwise, we cannot estimate the redshift because it is degenerate with the chirp mass. This well-known degeneracy can be broken by obtaining the redshift information from an electromagnetic counterpart such as the emission of a short Gamma-Ray Burst (GRB) (Capozziello et al. 2011; Abbott et al. 2017a) or the optical and spectroscopic localization of the host galaxy (Holz & Hughes 2005; Chen et al. 2018) though the latter will not be accurate for high redshift events (Cigarrán Díaz & Mukherjee 2022). Another solution, that has been recently proposed, relies on obtaining the redshift from the tidal deformation in a Binary Neutron Stars (BNS) merger (Messenger & Read 2012; Chatterjee et al. 2021). This solution may supply an estimation for the redshift with an accuracy ranging from 8% to 40%, depending on the choice of the equation of state.

Here, we want to study the following issues: first, we want to forecast the precision down to which ET will be able to constrain the Hubble constant  $H_0$  and the curvature parameter  $\Omega_{k,0}$  and its capability to resolve the aforementioned tensions using BNS signals. Several analyses have been carried out to measure the Hubble constant with ET (Zhao et al. 2011; Sathyaprakash et al. 2010; Cai & Yang 2017; D’Agostino & Nunes 2019; Yang et al. 2019; Bonilla et al. 2020; Belgacem et al. 2019; Zhang et al. 2019; Borhanian et al. 2020; Yu et al. 2021; Jin et al. 2021; Yang 2021; Jin et al. 2022a;

Leandro et al. 2022; Jin et al. 2022b; Alfradique et al. 2022), but they were considering only a flat- $\Lambda$ CDM model. Second, since ET will detect more than 20,000 BNS events/year at Signal-to-Noise ratio (SNR)  $\geq 9$  but only for  $\sim 0.1\%$  of them the electromagnetic counterpart can be observed (as we will show in Sect. 3), we want to analyse alternatives to the direct observation of the electromagnetic counterpart to investigate whether they can represent a viable way to achieve a better precision on the cosmological parameters. The manuscript is sectioned as follows: we first briefly introduce the fiducial cosmological model used to build the mock catalogs in Section 2. The details on the procedure used to build them are given in Section 3. In Section 4, we give the details of our statistical analysis used to forecast the precision of cosmological parameters achievable with ET, and in Section 5 we show all results. Finally, in Section 6, we summarize our results and give our main conclusions.

## 2 THE $\Lambda$ CDM COSMOLOGICAL MODEL

Let us start by briefly summarizing the  $\Lambda$ CDM cosmological model which is based on the Friedmann–Lemaître–Robertson–Walker (FLRW) metric

$$ds^2 = -c^2 dt^2 + a^2(t) \left[ \frac{dr^2}{1-kr^2} + r^2 (d\theta^2 + \sin^2\theta d\phi^2) \right], \quad (1)$$

where  $c$  is the speed of light,  $t$  is the cosmic time,  $a(t)$  is the scale factor whose evolution depends on the matter and energy contents of the Universe, and  $k = +1, -1, 0$  corresponds to a closed, open, and flat universe, respectively. From the Einstein equations, one can derive the Friedmann equations

$$H^2(t) = \frac{8\pi G}{3} \rho(t) - \frac{kc^2}{a^2(t)}, \quad (2)$$

$$\frac{\ddot{a}(t)}{a(t)} = -\frac{4\pi G}{3} \left( \rho(t) + \frac{3p(t)}{c^2} \right), \quad (3)$$

where  $G$  is the gravitational constant,  $H(t)$  is the Hubble parameter and  $\rho(t)$  is the energy-matter density given by  $\rho(t) = \rho_r(t) + \rho_m(t) + \rho_\Lambda$ . The first term represents the density of radiation, the second term represents the matter density and the last term represents the cosmological constant density. Then, defining the redshift  $z$  in terms of scale factor and using the definition of the critical energy density,  $\rho_c = \frac{3H^2}{8\pi G}$ , Eq. (2) can be recast as follows:

$$1 = \Omega_r(z) + \Omega_m(z) + \Omega_\Lambda + \Omega_k(z), \quad (4)$$

where the following definitions  $\Omega_i(z) \equiv \frac{\rho_i(z)}{\rho_c(z)}$  and  $\Omega_k(z) = \frac{-kc^2(1+z)^2}{H^2(z)}$  have been introduced. Finally, the Eq. (2) can be also recast as

$$\frac{H^2(z)}{H_0^2} \equiv E^2(z) = \Omega_{r,0}(1+z)^4 + \Omega_{m,0}(1+z)^3 + \Omega_{k,0}(1+z)^2 + \Omega_{\Lambda,0}, \quad (5)$$

which is required to compute the comoving distance

$$d_C(z) = D_H \int_0^z \frac{1}{E(z)} dz, \quad (6)$$

where  $D_H = \frac{c}{H_0}$  is the Hubble distance. Consequently, the luminosity distance is (Hogg 1999):

$$d_L(z) = S_k \left( \sqrt{|\Omega_{k,0}|} \frac{d_C}{D_H} \right) (1+z), \quad (7)$$

where

$$S_k \left( \sqrt{|\Omega_{k,0}|} \frac{d_c}{D_H} \right) = \begin{cases} \frac{d_H}{\sqrt{|\Omega_{k,0}|}} \sinh \left( \sqrt{|\Omega_{k,0}|} \frac{d_c}{D_H} \right) & \text{if } \Omega_{k,0} > 0 \\ d_c & \text{if } \Omega_{k,0} = 0 \\ \frac{d_H}{\sqrt{|\Omega_{k,0}|}} \sin \left( \sqrt{|\Omega_{k,0}|} \frac{d_c}{D_H} \right) & \text{if } \Omega_{k,0} < 0 \end{cases} \quad (8)$$

To build the mock catalogs of cosmological distances, we set as a *fiducial* cosmological model the  $\Lambda$ CDM with the following observational constraints:

$$H_0 = 67.66 \text{ km s}^{-1} \text{ Mpc}^{-1}, \quad \Omega_{k,0} = 0.0, \quad \Omega_{\Lambda,0} = 0.6889. \quad (9)$$

Since  $\Omega_{r,0} \sim 10^{-5}$  (Fixsen 2009), its contribution to the cosmic evolution of the Universe is negligible, in the range of redshift we will explore, compared the other components. Therefore, we set  $\Omega_{r,0} = 0$ . Finally, the contribution of the matter density,  $\Omega_{m,0}$ , is derived using Eq. (4) as  $\Omega_{m,0} = 1 - (\Omega_{\Lambda,0} + \Omega_{k,0})$ .

### 3 CONSTRUCTION OF MOCK SOURCE CATALOGS

Let us start by giving a schematic description of the main ingredients needed to build the mock catalogs:

- (i) the first step is to define the probability distribution  $p(z)$  of an event happening at redshift  $z$ . This probability distribution will depend on the astrophysics, *i.e.* the merger rate;
- (ii) the merger rate of BNS defines the rate density per unit of redshift in the observer frame, and it depends on the Star Formation Rate (SFR);
- (iii) one needs to define the mass distribution of the NS. We set it to be uniform in the interval  $[1, 2.5] M_{\odot}$ ;
- (iv) one needs to set the spatial distribution of the merger event of BNS. We set it to be isotropic on the sky angles  $\theta$  and  $\phi$ , and uniform on the orientation angle  $\cos i$  and the polarization  $\psi$ .

Once the previous ingredients have been defined, and using the *fiducial* cosmological model introduced in Section 2, we can extract the *fiducial* redshift of the GW source from the probability distribution  $p(z)$ . Then, we can predict the SNR,  $\rho$ , for ET using the expected one-sided noise power spectral density. Finally, we select events having SNR above a fixed threshold. Specifically, we will create three mock catalogs with SNR thresholds equal to  $[9, 12, 15]$  for each observational period fixed in one, five, and ten years. In total, we have nine mock catalogs containing all events that ET will be capable of detecting. From each one, we extract two sub-catalogs listing only the events of BNS merger that have a detected electromagnetic counterpart. Hence from each of the nine initial catalogs we finally obtain three catalogs, for a total of 27 mock catalogs.

#### 3.1 Probability distribution and merger rate of the GW events

The normalized probability distribution of GW events is defined as follows (Regimbau & Hughes 2009; Regimbau et al. 2012, 2014; Meacher et al. 2016; Cai & Yang 2017; Regimbau et al. 2017; Belgacem et al. 2019):

$$p(z) = \frac{R_z(z)}{\int_0^{z_{max}} R_z(z) dz}. \quad (10)$$

Here, we set the maximum observed redshift  $z_{max} = 10$  (Belgacem et al. 2019).  $R_z(z)$  is the merger rate density per unit of

redshift in the observer frame

$$R_z(z) = \frac{R_m(z) dV(z)}{1+z} \frac{dV(z)}{dz}, \quad (11)$$

where  $dV(z)/dz$  is the comoving volume element, and  $R_m(z)$  is the merger rate per volume in the source frame. The comoving volume can be written in terms of the comoving distance given in Eq. (6) as

$$\frac{dV(z)}{dz} = \frac{4\pi D_H d_C^2(z)}{E(z, \Omega_{k,0}, \Omega_{\Lambda,0})}. \quad (12)$$

On the other side, the merger rate per unit of volume at redshift  $z$  is related to the SFR through the time delay distribution  $P(t_d)$ . The latter is the probability distribution of the time delay,  $t_d$ , between the time at the formation of the massive progenitors ( $t_f$ ) and the time at which they merge ( $t_m$ ), *i.e.*  $t_d = t_f - t_m$ . The time delay distribution can be set to two different functional forms: (i) *power law* form  $P(t_d) \propto t_d^{-1}$  as suggested by population synthesis models (Tutukov & Yungelson 1994; Lipunov et al. 1995; de Freitas Pacheco et al. 2006; Belczynski et al. 2006; O’Shaughnessy et al. 2008), or (ii) *exponential* form  $P(t_d) \propto \tau^{-1} \exp(-t_d/\tau)$  as suggested by Vitale et al. (2019), with an e-fold time of  $\tau = 100$  Myr for the time delay distribution. Finally, the merger rate takes the following form

$$R_m^*(z) = \int_{t_{min}}^{t_{max}} R_f [t(z) - t_d] P(t_d) dt_d, \quad (13)$$

where  $t_{min} = 20$  Myr and  $t_{max}$  is the Hubble time (Meacher et al. 2015).  $R_f(t)$  is the formation rate of massive binaries and  $t(z)$  is the age of the Universe at the time of merger. Additionally, the formation rate of massive binaries follows the model for SFR (Regimbau & Hughes 2009), that can be set to the *Vangioni model* (Vangioni et al. 2015)

$$\text{SFR}(z) = \frac{\nu a \exp(b(z - z_m))}{a - b + b \exp(a(z - z_m))}, \quad (14)$$

with parameters  $a = 2.76$ ,  $b = 2.56$ ,  $z_m = 1.9$  and  $\nu = 0.16 M_{\odot}/\text{yr}/\text{Mpc}^3$ . Alternatively, the SFR can be also set to *Madau–Dickinson model* (Madau & Dickinson 2014)

$$\text{SFR}(z) = \frac{(1+z)^{\alpha}}{1 + [(1+z)/C]^{\beta}}, \quad (15)$$

with  $\alpha = 2.7$ ,  $\beta = 5.6$  and  $C = 2.9$ .

Finally, we normalize Eq. (13) by requiring that the value of  $R_m(z = 0)$  agrees with the most recent estimation of the local rate made by The LIGO Scientific Collaboration et al. (2021c):  $R_m(z = 0) = 105.5^{+190.2}_{-83.9} \text{ Gpc}^{-3} \text{ yr}^{-1}$ . Their estimation is inferred assuming that neutron stars masses range from 1 to 2.5  $M_{\odot}$ . Thus, the merger rate can be recast as:

$$R_m(z) = R_m(z = 0) \frac{R_m^*(z)}{R_m^*(z = 0)}. \quad (16)$$

In Figure 1, we show the normalized probability distribution of redshift (bottom panel) and the normalized BNS merger rate density (top panel) for different assumptions for SFR and time delay distribution. Once the probability distribution of GW events is built, we can extract the redshift of the GW events according to this distribution in framework of our *baseline* model, which adopts the *Vangioni model* for the SFR and the *power law* form of the time delay distribution. We will show in Section 5.3 that making other choices leads to similar constraints on the cosmological parameters.

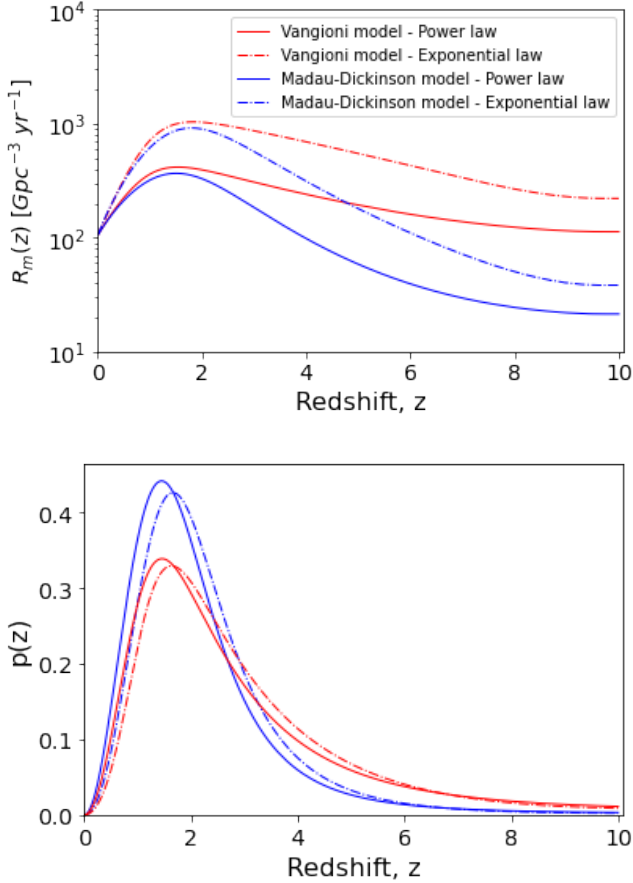


Figure 1: *Top*: The BNS merger rate as function of the redshift. *Bottom*: The normalized probability distribution of redshift. In both panels, we depict the Madau - Dickison model given in Eq. (15) (blue lines) and the Vangioni model given in Eq. (14) (red line). Furthermore, we show both a power law and an exponential time delay distribution as solid and dashed lines, respectively. In our *baseline* model, we adopt the Vangioni model for SFR and the power law time delay distribution (red solid line).

### 3.2 Detector sensitivity

The next step is to compute the SNR of the event detected by the ET. The observatory will have three independent interferometers and, hence, the combined SNR is (Finn 2001; Schutz 2011):

$$\rho = \sqrt{\sum_{i=1}^3 (\rho^{(i)})^2}. \quad (17)$$

Under the assumption of Gaussian noise, the  $i$ -th interferometer will have a SNR (Finn & Chernoff 1993)

$$\rho_i^2 = 4 \int_0^\infty \frac{|\tilde{h}(f)|}{S_{h,i}(f)} df, \quad (18)$$

where  $f$  is the GW frequency in the observer frame,  $S_{h,i}(f)$  is the one-sided noise power spectral density of  $i$ -th interferometer, and  $\tilde{h}$  is the Fourier transform of the GW strain amplitude (Blanchet et al. 1996):  $\tilde{h} = F_{+,i}\tilde{h}_+ + F_{\times,i}\tilde{h}_\times$ ; where  $\tilde{h}_+$  and  $\tilde{h}_\times$  are the GW strain amplitudes of + and  $\times$  polarizations, and  $F_{+,i}(\psi, \theta, \phi)$  and  $F_{\times,i}(\psi, \theta, \phi)$  are the so-called beam pattern functions (Zhao et al.

2011)

$$F_+^{(1)}(\theta, \phi, \psi) = \frac{\sqrt{3}}{4} \left[ (1 + \cos^2(\theta)) \cos(2\phi) \cos(2\psi) - 2 \cos(\theta) \sin(2\phi) \sin(2\psi) \right],$$

$$F_\times^{(1)}(\theta, \phi, \psi) = \frac{\sqrt{3}}{4} \left[ (1 + \cos^2(\theta)) \cos(2\phi) \sin(2\psi) + 2 \cos(\theta) \sin(2\phi) \cos(2\psi) \right], \quad (19)$$

$$F_{+, \times}^{(2)}(\theta, \phi, \psi) = F_{+, \times}^{(1)}(\theta, \phi + 2\pi/3, \psi),$$

$$F_{+, \times}^{(3)}(\theta, \phi, \psi) = F_{+, \times}^{(1)}(\theta, \phi + 4\pi/3, \psi),$$

where  $\phi$  and  $\theta$  are the sky localization angles, and  $\psi$  is the polarization angle. We select  $\phi$  and  $\psi$  angles randomly from a uniform distribution in the range  $[0, 2\pi]$ , whereas  $\theta$  belongs to the range  $[0, \pi]$ . At quadrupolar order, the GW strain amplitudes of the polarization states can be written as (Finn & Chernoff 1993)

$$\tilde{h}_+ = \frac{1}{\pi^{2/3}} \left( \frac{5}{24} \right)^{1/2} \frac{c}{d_L} \left( \frac{GM_c}{c^3} \right)^{5/6} f^{-7/6} \left( \frac{1 + \cos i^2}{2} \right), \quad (20)$$

$$\tilde{h}_\times = \frac{1}{\pi^{2/3}} \left( \frac{5}{24} \right)^{1/2} \frac{c}{d_L} \left( \frac{GM_c}{c^3} \right)^{5/6} f^{-7/6} \cos i, \quad (21)$$

where  $M_c$  is the observed chirp mass defined as a combination of individual masses  $m_1$  and  $m_2$ ,  $M_c = (1+z) \frac{(m_1 m_2)^{3/5}}{(m_1 + m_2)^{1/5}}$ . Since the dominant contribution to SNR in a BNS event comes from the inspiral phase (Finn & Chernoff 1993), the SNR can be written as

$$\rho_i^2 = \frac{5}{6} \frac{(GM_{c,obs})^{5/3} \mathcal{F}_i^2}{c^3 \pi^{4/3} d_L^2(z)} \int_{f_{lower}}^{f_{upper}} \frac{f^{-7/3}}{S_{h,i}(f)} df, \quad (22)$$

where

$$\mathcal{F}_i^2 = \left( \frac{1 + \cos^2 i}{2} \right)^2 F_{+,i}^2 + \cos^2 i F_{\times,i}^2, \quad (23)$$

and  $\cos^2 i$  is the cosine square of the inclination angle. The latter is also selected randomly from a uniform distribution ranging from zero to  $\pi$ . The upper limit of the integration,  $f_{upper}$ , is related to the frequency of the last stable orbit (LSO),  $f_{LSO}$ , which marks the end of the inspiral phase and the onset of the final merger (Maggiore 2007)

$$f_{upper} = 2f_{LSO} = \frac{c^3}{(6\sqrt{6}\pi M_{obs})G}, \quad (24)$$

where  $M_{obs} = (1+z)(m_1 + m_2)$  is the observed total mass in the reference frame of the observer. The lower cutoff of the integration,  $f_{lower}$ , depends on the detector. In case of the ET the lower limit frequency is  $f_{lower} = 1$  Hz (Hild et al. 2011). Finally,  $S_h(f)$  is the latest sensitivity curve made available by the ET collaboration<sup>1</sup>. Once the SNR is computed, we can build our mock catalogs by selecting all the events above a given threshold.

### 3.3 The mock catalogs

The detection rate of sources depends on the sensitivity, observing time, and duty cycle of the GW detector network, *i.e.*, the time percentage of the detectors in science mode (Regimbau et al. 2015).

<sup>1</sup> The latest power spectral density  $S_h(f)$  can be downloaded at <https://apps.et-gw.eu/tds/?content=3&r=14065>.

**Table 1.** Numbers of GW events from BNS merger recorded in each mock catalog depending on the threshold in the SNR and the total number of observational years.

Years	SNR = 9		SNR = 12		SNR = 15	
	# events	$z_{max}$	# events	$z_{max}$	# events	$z_{max}$
1	52309	6.23	29594	3.97	17235	2.65
5	260088	6.77	146512	4.03	85595	2.86
10	521552	6.91	294284	4.05	171270	2.86

We set the duty-cycle of the ET to 80% as in Ref. (Regimbau et al. 2015). In other words, ET will detect the 80% of the total number of events. The latter is estimated integrating the Eq. (11) over the redshift interval  $z = [0, 10]$  and multiplying it by 1, 5 or 10 years of observations. Additionally, only events above a given threshold are retained. More specifically, we set three different thresholds in SNR equal to 9, 12, and 15. Finally, we add a Gaussian noise component,  $\mathcal{N}(d_L^{fid}, \sigma_{d_L})$ , to our estimations of the luminosity distances  $d_L^{fid}$  based on the *fiducial* cosmological model. The variance  $\sigma_{d_L}$  accounts for different sources of uncertainties:

$$\sigma_{d_L} = \sqrt{\sigma_{inst}^2 + \sigma_{delens}^2 + \sigma_{pec}^2}. \quad (25)$$

The first term  $\sigma_{inst}$  is related to the instrumental error and is proportional to  $1/\rho$  (Cutler & Flanagan 1994; Dalal et al. 2006):

$$\sigma_{inst} = \frac{2}{\rho} d_L(z). \quad (26)$$

The factor two accounts for the degeneration between  $\rho$  and the inclination angle, which may differ for each event. However, the detection of the electromagnetic counterpart breaks the degeneracy between distance and inclination angle and improves the accuracy by a factor of two (Nissanke et al. 2010). Anyway, to be conservative, we retained the factor two in  $\sigma_{inst}$ .

The second contribution to the total uncertainty,  $\sigma_{lens}$ , accounts for the weak lensing distortions (Hirata et al. 2010; Tamanini et al. 2016)

$$\sigma_{lens} = 0.066 \left( \frac{1 - (1+z)^{-0.25}}{0.25} \right)^{1.8} d_L(z). \quad (27)$$

Nevertheless, the future detectors such as the Extremely Large Telescope will estimate the lensing magnification distribution along the line of sight of the GW event (Shapiro et al. 2010), and they will allow to reduce the uncertainty due to weak lensing by applying a de-lensing factor  $F_{delens}(z)$  (Speri et al. 2021)

$$\sigma_{delens} = F_{delens}(z) (\sigma_{d_L}(z))_{lens}, \quad (28)$$

where  $F_{delens}(z) = 1 - \frac{0.3}{\pi/2} \arctan \frac{z}{z_*}$ , with  $z_* = 0.073$ .

The last contribution to the total uncertainty,  $\sigma_{pec}$ , is related to the peculiar velocities, and can be estimated by mean of a fitting formula (Kocsis et al. 2006)

$$\sigma_{pec} = \left[ 1 + \frac{c(1+z)^2}{H(z)d_L(z)} \right] \frac{\sqrt{\langle v^2 \rangle}}{c} d_L(z), \quad (29)$$

where we set the averaged peculiar velocity  $\langle v^2 \rangle$  to 500 km/s, in agreement with the observed values in galaxy catalogs (Cen & Ostriker 2000).

In Table 1, we report the number of events and the maximum observed redshift corresponding to each catalog. We built a total of nine catalogs corresponding to the one, five and ten years of

observing mode, and to SNR equal to 9, 12, and 15. The rate of events that we have obtained is comparable with the one expected for ET, as shown in Maggiore et al. (2020). In Figure 2, we illustrate the observed events distribution as function of the redshift. The left, central, and right panels correspond to the SNR thresholds 9, 12, and 15, respectively. Each panel depicts the redshift distribution obtained after one, five and ten years of observations with dark red, red, and light red colors as shown in the legend.

### 3.4 Detection of the electromagnetic counterpart with THESEUS

On August 17, 2017 at 12:41:04 UTC a new era of gravitational and multi-messenger astronomy began. The Advanced LIGO (aLIGO) and Advanced Virgo (aVIRGO) GW detectors observed the first merger of a BNS, GW170817, with the simultaneous detection of the Gamma-Ray Burst (GRB) 170817A associated with a GW event (Abbott et al. 2017b). This event was extremely important not only to constrain astrophysical scenarios for the production of a GRB (Abbott et al. 2017b), but also to constrain fundamental physics and modified gravity theories. For instance, the tiny time lag detected between the GWs and their electromagnetic counterpart served to rule out several modified theories of gravity where GWs and photons travel at two different speeds, and to reduce the parameter space of the Effective Field Theory of Dark Energy (Baker et al. 2017; Creminelli & Vernizzi 2017; Ezquiaga & Zumalacárregui 2017; Sakstein & Jain 2017; Wang et al. 2017; Wei et al. 2017; Amendola et al. 2018; Cai et al. 2018; Crisostomi & Koyama 2018; Kreisch & Komatsu 2018). Hence, it results extremely important to know how many events that will be detected by ET, will also be detected by forthcoming Gamma-Ray and X-Ray satellites. In the following, we will focus on the Transient High Energy Sources and Early Universe Surveyor (THESEUS) satellite that could overlap with ET and provide the electromagnetic counterpart of the GW events (Amati et al. 2018; Stratta et al. 2018; Amati et al. 2021; Ciolfi et al. 2021; Ghirlanda et al. 2021; Rosati et al. 2021).

Once the GW catalogs have been built, we look for those events with a detectable electromagnetic counterpart in order to obtain the corresponding redshift of the event and break the mass-redshift degeneracy (Finn & Chernoff 1993) to use the binary NS as standard (bright) sirens. As mentioned above, we focus on the observational specifications of the THESEUS satellite and, following Yang (2021), we simulate the observed photon flux of the GRB events associated with a GW event through the luminosity distance by sampling the luminosity probability distribution  $\phi(L)$ . Then, if the observed flux is above the given threshold, we retain the event. There are two ways of identifying the source of the electromagnetic counterpart in the sky. On one side, one can localize the source and follow-up it with optical telescopes, as done to detect the electromagnetic counterpart of the event GW170817. ET will localize the most of the detectable BNS at a distance  $\leq 200$  Mpc to within a 90% credible region of 100 deg<sup>2</sup> (Chan et al. 2018; Zhao & Wen 2018; Li et al. 2022). On the other side, even without a precise sky localization, joint observations are possible. Indeed, the time coincidence of the GW event with a short GRB can be used and then the redshift can be determined from the X-ray afterglow.

Starting from the mock catalogs of the GW events, we want to extract those events having a detected electromagnetic counterpart. To this aim, we need to know observational features of the short GRBs such as the viewing angle and the sharpness of the angular profile. Thus, we assume the following luminosity profile of the jet (Resmi

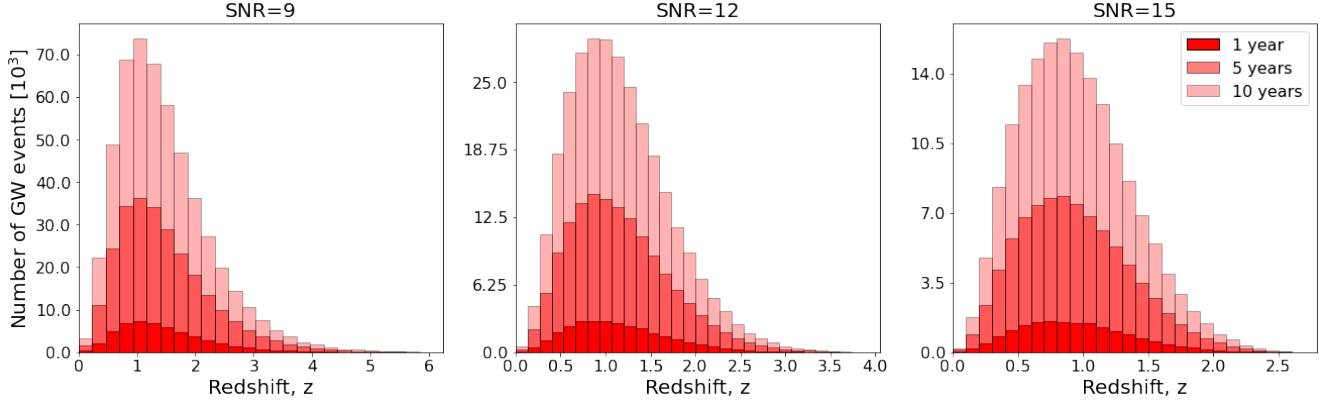


Figure 2: Distribution of the expected rate of detection of GW events from BNS merger with ET. Left, central, and right panels illustrate the detection rate for  $\text{SNR} > [9, 12, 15]$ , respectively.

et al. 2018)

$$L(\theta_V) = L_c e^{-\frac{\theta_V^2}{2\theta_c^2}}, \quad (30)$$

where  $L(\theta)$  is the luminosity per unit of solid angle,  $\theta_V$  is the viewing angle and  $L_c$  and  $\theta_c$  are the structure parameters that define the sharpness of the angular profile. A jet with a large  $\theta_c$  is similar to a uniform jet. Following the analysis made by Howell et al. (2019), we set  $\theta_c = 4.7^\circ$ . The value of  $L_c$  is related to the peak luminosity of each burst,  $L_p$ , by the relation  $L_c = \frac{L_p}{4\pi} \text{ erg s}^{-1} \text{ sr}^{-1}$  (Resmi et al. 2018). We then assume that  $L_p$  is distributed following a standard broken power law (Wanderman & Piran 2015)

$$\Phi(L_p) \propto \begin{cases} \left(\frac{L_p}{L_*}\right)^\alpha & (L_{min} < L_p < L_*), \\ \left(\frac{L_p}{L_*}\right)^\beta & (L_p > L_*), \end{cases} \quad (31)$$

where  $L_p$  is the isotropic rest frame luminosity in the  $1 - 10^4$  keV energy range, and  $L_*$  represents a characteristic luminosity that separates the low and high regimes of the luminosity function encoded in the value of the coefficients  $\alpha$  and  $\beta$ . Finally,  $L_{min}$  is the low end cutoff. We set these parameters to the values given by Wanderman & Piran (2015)  $\alpha = -1.95$ ,  $\beta = -3$ ,  $L_* = 2 \times 10^{52} \text{ erg s}^{-1}$ , and  $L_{min} = 10^{49} \text{ erg s}^{-1}$ .

Next, by sampling the luminosity distribution function in Eq. (31), we get a value of  $L_p$  for each burst that must be converted to an observed flux. However, the relation flux-luminosity requires two correction factors (Mészáros et al. 2011):

$$F(\theta_V) = \frac{(4\pi L(\theta_V))(1+z)}{4\pi d_L^2 k(z) b}. \quad (32)$$

The first correction term,  $b$ , is an energy normalization due to scaling of observed photon flux to account for the missing fraction of the gamma-ray energy seen in the detector band:

$$b = \frac{\int_{1 \text{ keV}}^{10000 \text{ keV}} EN(E)dE}{\int_{E1}^{E2} N(E)dE}, \quad (33)$$

where  $E1$ ,  $E2$  are the extreme of the detector's energy window, and  $N(E)$  is the band function. The second correction term,  $k(z)$ , is due to redshifted photon energy, also called  $k$ -correction, and it is given

by

$$k(z) = \frac{\int_{E1}^{E2} N(E)dE}{\int_{E1(1+z)}^{E2(1+z)} N(E)dE}. \quad (34)$$

The band function  $N(E)$  is given by a phenomenological fit to the observed GRB photon spectrum (Band et al. 1993)

$$N(E) = \begin{cases} N_0 \left(\frac{E}{100 \text{ keV}}\right)^{\alpha_B} \exp\left(-\frac{E}{E_0}\right) & (E < E_b), \\ N_0 \left(\frac{E_b}{100 \text{ keV}}\right)^{\alpha_B - \beta_B} \exp(\beta_B - \alpha_B) \left(\frac{E}{100 \text{ keV}}\right)^{\beta_B} & (E > E_b), \end{cases} \quad (35)$$

where  $E_b = (\alpha_B - \beta_B)E_0$  and  $E_p = (\alpha_B + 2)E_0$ . We set  $\alpha_B = -0.5$ ,  $\beta_B = -2.25$  and a peak energy  $E_p = 800$  keV in the source frame as in (Nava et al. 2011). Finally, the factor  $(1+z)$  in the Eq. (32) is related to the fact that the flux is measured in units of  $\left[\frac{\text{photon}}{\text{cm}^2 \text{ s}}\right]$  (Mészáros et al. 2011).

THESEUS satellite will detect a 15 - 35 coincident short GRB per year (Stratta et al. 2018), which represent only the  $\sim 0.08\%$  of the expected rate of GW events detected by ET at  $\text{SNR} > 9$  (see Table 1). We set the duty cycle of the THESEUS satellite to 80% (Stratta et al. 2018) mainly due to a reduction of observing time owing to the passage through the Southern Atlantic Anomaly, a sky coverage fraction of 0.5, and a flux limit  $F_{min} = 0.2 \text{ photon cm}^{-2} \text{ s}^{-1}$  in the 50 - 300 keV. This configuration favors a source localization with a precision of  $\sim 5$  arcmin, but only within the central 2 sr of the X-Gamma ray Imaging Spectrometer (XGIS) field of view (FOV) (Stratta et al. 2018). Thus, we follow Belgacem et al. (2019) setting the effective number of the detected sources to 1/3 of the total number of detected short GRBs, and analysing two cases: first, the *optimistic* case in which all the events detected by XGIS have a measured redshift; and second, the *realistic* case in which the redshift is measured only for sources that are localized with a precision of  $\sim 5$  arcmin. In Table 2, we report the data for the *optimistic* and *realistic* cases. We estimate a rate of order  $5 \div 10$  in the *realistic* case, a factor at least  $\sim 3$  lower than predicted for the THESEUS mission by Stratta et al. (2018); while in the *optimistic* case we estimate a rate of order  $16 \div 31$ , a factor at least  $\sim 1.6$  to  $\sim 2$  lower than predicted for the THESEUS mission by Belgacem et al. (2019). Such differences are rather expected since we assume a different BNS rate function with respect to Stratta et al. (2018), and a lower value of the local rate  $R_m(z=0)$  with respect to Belgacem et al. (2019). We checked that

Optimistic Case						
Years	SNR = 9		SNR = 12		SNR = 15	
	# events	$z_{max}$	# events	$z_{max}$	# events	$z_{max}$
1	31	2.66	25	1.81	16	1.36
5	166	4.03	125	2.85	97	2.15
10	332	5.08	249	2.85	204	2.41

Realistic Case						
Years	SNR = 9		SNR = 12		SNR = 15	
	# events	$z_{max}$	# events	$z_{max}$	# events	$z_{max}$
1	10	2.66	8	1.18	5	1.49
5	55	3.00	41	1.95	32	2.15
10	110	4.13	83	2.60	68	2.19

**Table 2.** Numbers of GW events with electromagnetic counterpart recorded in each mock catalog depending on the threshold in the SNR and the total number of observational years. We report numbers for both the *optimistic* and the *realistic* cases.

using the same model of [Stratta et al. \(2018\)](#) and the same value of  $R_m(z=0)$  with respect to [Belgacem et al. \(2019\)](#), we recover their estimated number of events. Finally, for the sake of completeness, we illustrate in Figure 3 the observed event distribution as a function of the redshift for both the *optimistic* and the *realistic* cases in the upper and bottom row, respectively. The left, central, and right panels correspond to the SNR thresholds 9, 12, and 15, respectively. In each panel, we depict the redshift distribution obtained after one, five and ten years of observations with dark red, red, and light red colors as shown in the legend.

We checked that changing the model of the luminosity profile of the jet in Eq. (30) does not change remarkably the number of the detected events. We have compared the model in Eq. (30) with a two-component jet model and a structured jet model in which the energy is a function of the jet angle outside a uniform core ([Lamb & Kobayashi 2017](#)). Our results indicates that, using Eq. (30), 10 and 31 events are detected in the realistic and optimistic cases, respectively. Whereas, using a two-component jet model one detects 12 and 36 events, respectively. And, finally, using a structured jet one detects 12 and 37 events, respectively.

#### 4 BAYESIAN STATISTICAL ANALYSIS

To evaluate the accuracy down to which ET will be able to constrain cosmological parameters, we carry out a statistical analysis employing a Monte Carlo Markov Chain (MCMC) algorithm. We will use the emcee Python package ([Foreman-Mackey et al. 2013](#)) to constrain the cosmological parameters by fitting the luminosity distance for all our mock catalogs, *i.e.* with and without the detection of an electromagnetic counterpart. Using the Bayes' theorem, we express the posterior distribution,  $p(\mathcal{H}|\mathbf{d})$ , of the cosmological parameters  $\mathcal{H} = \{H_0, \Omega_{k,0}, \Omega_{\Lambda,0}\}$ , in terms of the likelihood function,  $p(\mathbf{d}|\mathcal{H})$ , and the prior distribution  $p_0(\mathcal{H})$  ([Padilla et al. 2021](#)):

$$p(\mathcal{H}|\mathbf{d}) \propto p(\mathbf{d}|\mathcal{H})p_0(\mathcal{H}). \quad (36)$$

Here, we have labeled the dataset with  $\mathbf{d} \equiv \{d_i\}_{i=1}^N$ , where  $N$  is the number of observations. Furthermore, the uniform prior distributions for all the model parameters are:  $H_0 \in \mathcal{U}(35, 85)$ ,  $\Omega_{k,0} \in \mathcal{U}(-1, 1)$  and  $\Omega_{\Lambda,0} \in \mathcal{U}(0, 1)$ . It is worth stressing that in our analysis, we

neglect the contribution of source spin to the amplitude of the signal ([Poisson & Will 1995](#); [Baird et al. 2013](#)). Finally, the total likelihood of the GW events is the product of the single event likelihood:

$$p(\mathbf{d}|\mathcal{H}) = \prod_{i=1}^N p(d_i|\mathcal{H}). \quad (37)$$

We will examine three different cases: (I) including the redshift information from the electromagnetic signal; (II) including selection effects due to the cut in SNR and flux with respect to (I); and, finally, (III) using all the GW events detected by the ET, even those without electromagnetic counterpart, the so called *dark sirens*. Specifically:

(I): the information about the redshift of the source comes from the detection of the electromagnetic counterpart allowing to break the mass-redshift degeneracy. In such a case, we define and use the following log-likelihood

$$-\log p(d_i|\mathcal{H}) = \frac{1}{2} \left( \frac{d_i - d_L^{th}(z_i, \mathcal{H})}{\sigma_{d_i}} \right)^2 + \log(2\pi\sigma_{d_i}), \quad (38)$$

where  $d_L^{th}(z_i, \mathcal{H})$  is the theoretical luminosity distance given by the Eq. (7),  $d_i \equiv d_L(z_i)$ ,  $z_i$  is the redshift of coincident GRB (we assume it perfectly known), and  $\sigma_{d_i}$  are the mock data and the corresponding error bars, respectively.

(II): As in the previous case, the information about the redshift is known. We use a hierarchical Bayesian framework to include selection effects ([Mandel et al. 2019](#); [Vitale et al. 2020](#)). Generally speaking, the posterior probability distribution of a single event in presence of selection effects is ([Mandel et al. 2019](#))

$$p(d_i|\mathcal{H}) = \frac{\int p(d_i|\lambda)p_{pop}(\lambda|\mathcal{H})d\lambda}{\int p_{det}(\lambda)p_{pop}(\lambda|\mathcal{H})d\lambda}, \quad (39)$$

where  $\lambda$  can be whatever parameter related to the GW event, such as spins, masses, and redshift among the others,  $p(d_i|\lambda)$  is the likelihood for detecting an event at the distance  $d_i$  given the set of parameters  $\lambda$ ,  $p_{det}(\lambda|\mathcal{H})$  is the probability of detecting a event with an intrinsic parameter  $\lambda$  given the set of parameters  $\mathcal{H}$  and, finally,  $p_{pop}(\lambda|\mathcal{H})$  is a population modelled prior distribution. The denominator is a normalization factor that takes into account the selection effects. In our catalogs, we have two selection effects that may affect final constraints: the first is generated by the selection in the SNR; and the second, by the selection in electromagnetic flux. Therefore, the probability distribution can be written as ([Del Pozzo 2012](#); [Mandel et al. 2019](#); [Ye & Fishbach 2021](#))

$$p(d_i|\mathcal{H}) = \frac{\int p(d_i|D_L)p_{pop}(D_L|z_i, \mathcal{H})dD_L}{\int p_{det}(D_L)p_{pop}(D_L|z_i, \mathcal{H})dD_L}, \quad (40)$$

where  $p_{pop}(D_L|z_i, \mathcal{H}) = \delta(D_L - d_L^{th}(z_i, \mathcal{H}))$  ([Del Pozzo 2012](#)). The integration of the previous equation leads to

$$p(d_i|\mathcal{H}) = \frac{p(d_i|d_L^{th}(z_i, \mathcal{H}))}{p_{det}(d_L^{th}(z_i, \mathcal{H}))}, \quad (41)$$

where the numerator is given by Eq. (38), and the denominator gives the joint probability of detecting an event and the corresponding short GRB above a certain threshold in SNR and flux:

$$p_{det}(d_L^{th}(z_i, \mathcal{H})|\rho_i > \rho_t, F_i > F_{min}) = p_{det}^{\rho_i} p_{det}^{F_i}. \quad (42)$$

The first term gives the probability of detecting an event at redshift  $z_i$  and with  $\text{SNR} = \rho_i$  above a certain threshold  $\rho_t$ . From the relation  $\rho_i \propto d_i^{-1}$ , we get

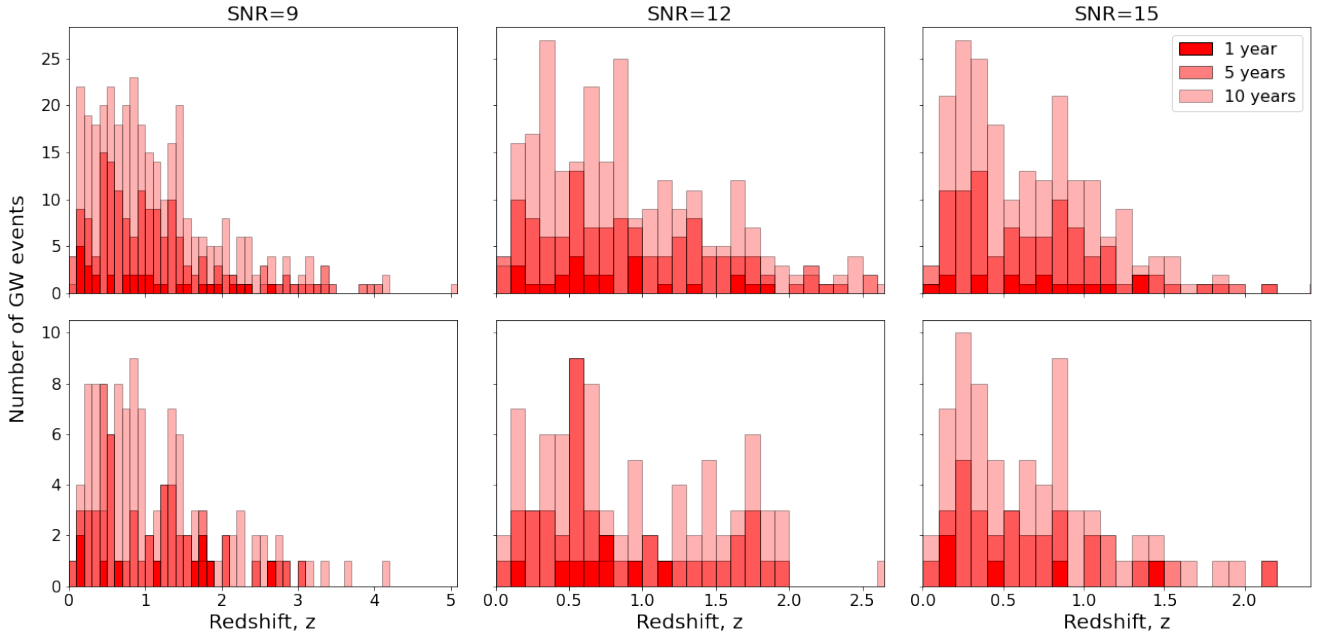


Figure 3: Distribution of the expected rate of detection of GW events with an electromagnetic counterpart for both the *optimistic* and the *realistic* cases in upper and lower row, respectively. Left, central, and right panels illustrate the detection rate for  $\text{SNR} > [9, 12, 15]$ , respectively.

$$\begin{aligned}
 p_{det}^{\rho_i} &\equiv p_{det}(d_L^{th}(z_i, \mathcal{H}) | \rho_i > \rho_t) = \int_{\rho_t}^{+\infty} d\rho_i p(\rho_i | d_L^{th}(z_i, \mathcal{H})) \\
 &= \frac{1}{2} \left[ 1 + \text{erf} \left( \frac{d_L^{th}(z_i, \mathcal{H})}{\sqrt{2}\sigma_{d_i}} (\rho_i - 1) \right) \right]. \quad (43)
 \end{aligned}$$

The second term gives the probability of detecting an event above a certain threshold in flux with a given threshold in SNR. Since the luminosity distance is Gaussian distributed and  $F_i \propto d_i^{-2}$ , it follows

$$\begin{aligned}
 p_{det}^{F_i} &\equiv p_{det}(d_L^{th}(z_i, \mathcal{H}), F_i > F_{min} | \rho_i > \rho_t) \\
 &= \int_{F_{min}}^{+\infty} dF_i p(F_i | d_L^{th}(z_i, \mathcal{H})) \\
 &= \frac{1}{4} \left[ 1 + \text{sign}(\Delta_i) \text{erf} \left( \frac{\Delta_i}{\sqrt{2}\sigma_{d_L}} \right) \right], \quad (44)
 \end{aligned}$$

where, for sake of convenience, we have defined

$$\Delta_i = \sqrt{\frac{L_i}{4\pi F_{min}}} - d_L^{th}(z_i, \mathcal{H}), \quad (45)$$

with  $L_i$  the luminosity of short GRB.

(III): As already mentioned in the Introduction, the electromagnetic counterpart will be detected only for the  $\sim 0.08\%$  of the total number of events detected by the ET. Therefore, it is mandatory to investigate which precision can be achieved using all the remaining data although one has to marginalize on the redshift. One way is to marginalize over the redshift of the potential host galaxies obtained by the localization of the GW event (Schutz 1986; MacLeod & Hogan 2008; Del Pozzo 2012). This approach is called statistical host identification technique. By applying this methodology to the 47 GW events with detected  $\text{SNR} > 11$  reported in the third LIGO-Virgo-KAGRA Gravitational Wave Transient Catalog (The LIGO Scientific Collaboration et al. 2021b), the The LIGO Scientific Collaboration et al. (2021a) obtain  $H_0 = 68_{-6}^{+8} \text{ km s}^{-1} \text{ Mpc}^{-1}$ . In addition to the latter method, one can use the three-dimensional cross-correlation

technique for GW sources and galaxies (Mukherjee et al. 2021a,b). Both approaches rely on the following key aspects: (a) the source sky localization error, (b) the luminosity distance uncertainty, (c) the overlapping sky area between GW sources and galaxy surveys, (d) the accurate redshift estimation of galaxies, and (e) the redshift distribution of galaxies (Cigarrán Díaz & Mukherjee 2022). In particular, increasing the error on the sky localization suppresses the cross-correlation (Mukherjee et al. 2021a). Hence, the nearby GW sources have better sky localization and provide a more precise estimation of the redshift. On the other hand, the statistical host identification technique depends on whether the host galaxy of the GW source is present in a galaxy catalog (Gray et al. 2020; Bera et al. 2020). However, even without an electromagnetic counterpart or a complete galaxies catalog or a galaxy surveys with higher galaxy number density, if the redshift distribution of the population of the GW events is known, for instance using population synthesis simulations, one can extract cosmological information (Ding et al. 2019; Ye & Fishbach 2021). Indeed, the probability of detecting an event at redshift  $z_i$  in a specified cosmological model is given by:

$$\begin{aligned}
 p(d_i | \mathcal{H}) &= \int_0^{z_{max}} p(d_i, z_i | \mathcal{H}) dz_i \\
 &= \int_0^{z_{max}} p(d_i | d_L^{th}(z_i, \mathcal{H})) p_{obs}(z_i | \mathcal{H}) dz_i. \quad (46)
 \end{aligned}$$

The probability prior distribution of the redshift,  $p_{obs}(z_i | \mathcal{H})$ , is obtained from the observed events and already includes detector selection effects (Ding et al. 2019), since it is related to the distribution  $p(z)$  in Eq. (10) through the condition that  $\rho > \rho_t$ . Furthermore, the likelihood  $p(d_i | d_L^{th}(z_i, \mathcal{H}))$  is given in Eq. (38).

Additionally, it has been recently shown that the redshift of a GW event can be obtained from the measurements of the tidal effects in BNS (Messenger & Read 2012; Ghosh et al. 2022). Having such a prior estimation of the redshift directly from the waveform would allow to assume a Gaussian prior distribution on redshift,  $p_{obs}(z_i | \mathcal{H}) = \mathcal{N}(z_i^{obs}, \sigma_{z_i})$ , that would be centered in its corre-



sponding estimated value  $z_i^{obs}$  with a variance given by statistical error  $\sigma_{z_i}$  (Jiang & Yagi 2021).

In our analysis, we refer to *dark sirens* when using all the events without the electromagnetic counterpart, assuming known the redshift prior distribution from population synthesis simulations and/or the measure of the tidal deformability parameter. In this case, we adopt the likelihood defined in Eq. (46).

## 5 RESULTS

We have built mock catalogs of the luminosity distance extracted by the GW events that will be detected by the forthcoming ET throughout one, five and ten years of observations. Our *baseline* model is a flat- $\Lambda$ CDM with the fiducial values of parameter  $H_0$ ,  $\Omega_k$ , and  $\Omega_\Lambda$  given in Eq. (9). In our mock catalogs, we retained only the events with a SNR above a given threshold, *i.e.* SNR > [9, 12, 15]. Therefore, we finally have nine mock catalogs with the number of events ranging from  $\sim 10^4$  to  $\sim 5 \times 10^5$  depending on SNR and on the years of observations, as shown in Table 1. Additionally, we extract from each catalog those events that will have an electromagnetic emission detectable by the THESEUS mission. Therefore, we create other 18 mock catalogs only containing GW events with a detected electromagnetic counterpart. As reported in Table 2, to build nine of those catalogs, we assume that all GW events detectable by THESEUS will be effectively detected (*optimistic case*), while to build the other nine catalogs we assume that the electromagnetic counterpart is detected in 1/3 of the total number of detectable events (*realistic case*). Then, we use a MCMC algorithm to forecast the precision down to which ET would recover cosmological parameters. We carry out three analyses: (I) considering only the events with a detected electromagnetic counterpart, (II) the same but including selection effects as explained in the previous section, and (III) including *dark sirens*. We will refer our discussions to the mock catalog that collects all the events with SNR > 9 detected throughout ten years of observations (hereby called *reference catalog*).

### 5.1 Analysis of GW events with a detected electromagnetic counterpart

Table 3 reports the median value and the 68% confidence level of the posterior distributions of the parameters of our *baseline* model for each SNR and for one, five and ten years of observations. Those results are obtained by applying our pipeline to the mock catalog of GW events with a detected electromagnetic counterpart in both *realistic* and *optimistic* cases. It is worth remembering that the number of events we predicted to be detected ranges from a few events at redshift around two to at most  $\sim 110$  events at a maximum redshift of  $\sim 4$  in the *realistic* case. While, in the *optimistic* case, we found a number of events ranging from  $\sim 30$  events to  $\sim 330$  events at a maximum redshift of  $\sim 5$  (as shown in Table 2). Therefore, final results will be affected by the limited number of events and the relatively small redshift at which sometimes they are located. Said that, we predicted that the Hubble constant may be detected with an accuracy at most of  $\sigma_{H_0} \approx 0.85$  and  $0.40 \text{ km s}^{-1} \text{ Mpc}^{-1}$  for our *reference catalog* representing an uncertainty at level of  $\sim 0.7\%$  and  $\sim 0.4\%$  in the *realistic* and *optimistic* cases, respectively. On the other hand, in the same analysis, the curvature parameter  $\Omega_{k,0}$  may be detected with an accuracy at most of  $\sigma_{\Omega_{k,0}} \approx 0.17$  or  $0.09$ , while the cosmological constant density with an accuracy at most of  $\sigma_{\Omega_{\Lambda,0}} \approx 0.14$  or  $0.07$  in the *realistic* and *optimistic* cases, respectively. We show in Figure 4 the contour plots corresponding to the 68%, 95% and 99.7%

of confidence level obtained from the posterior distributions of the parameters of our *baseline* model. The left and right panels show the analysis in the *realistic* and *optimistic* case, respectively, carried out on the *reference catalog*. We depict the input value of the cosmological parameters as a vertical red line in the histograms and a red point in the contour plot. While, in the histograms, the vertical dashed line indicates the median value and the shaded band indicates the  $1\sigma$  confidence interval. The true values of the cosmological parameters are always recovered within  $1\sigma$ . For sake of completeness we report all the other contour plots in the Appendix A of Supplementary Materials (SM).

In addition to the previous results, we repeat all the analyses including the selection effects as discussed in Section 4. We note that including selection effects has a very small impact on the final results of the order of a few percent. In Figure 5 we show the contour plots corresponding to the 68%, 95% and 99.7% of confidence level obtained from the posterior distributions of the parameters of our *baseline* model. Panels, lines and colors follow the same design of Figure 4, while the true values of the cosmological parameters are again recovered within  $1\sigma$ . For sake of completeness, we report all the other contour plots in the Appendix B of SM.

We can compare our results with the analysis of non-flat  $\Lambda$ CDM cosmology, carried out by Di Valentino et al. (2021b); Akarsu et al. (2021), based on the CMB power spectrum, Cosmic Chronometers (CC) and Type Ia Supernovae (SNIa). Di Valentino et al. (2021b) use the CMB power spectrum together with the Baryonic Acoustic Oscillation (BAO) data and the Pantheon sample of SNIa data. When using CMB+BAO data, they constrained the Hubble constant with an accuracy on  $\sigma_{H_0} \approx 1.7 \text{ km s}^{-1} \text{ Mpc}^{-1}$  and the curvature parameter with an accuracy on  $\sigma_{\Omega_{k,0}} \approx 0.005$ , which degrade to  $\sigma_{H_0} \approx 4.4 \text{ km s}^{-1} \text{ Mpc}^{-1}$  and  $\sigma_{\Omega_{k,0}} \approx 0.02$  when using CMB+SNIa. On the other hand, the accuracy on Hubble constant, from Akarsu et al. (2021), is  $\sigma_{H_0} \approx 3 \text{ km s}^{-1} \text{ Mpc}^{-1}$  and  $\sigma_{H_0} \approx 10 \text{ km s}^{-1} \text{ Mpc}^{-1}$ . While the accuracy on the curvature parameter is  $\sigma_{\Omega_{k,0}} \approx 0.16$  and  $\sigma_{\Omega_{k,0}} \approx 0.14$ , using the CC and Pantheon sample of SNIa, respectively. Our results from the *reference catalog* show an improvement of  $\sim 40\%$  and  $\sim 76\%$  in the accuracy on the Hubble constant, in the *realistic* and *optimistic* cases, respectively, with respect to the best scenario of Di Valentino et al. (2021b). While, with respect to Akarsu et al. (2021), we predict to improve the accuracy on the Hubble constant of a factor  $\sim 3.5$  and  $\sim 7.5$  in the *realistic* and *optimistic* cases, respectively. Moreover, we are not competitive on the accuracy predicted on the curvature parameter by Di Valentino et al. (2021b). However, for the *realistic* case, we predict an accuracy of the same order of Akarsu et al. (2021), whereas for *optimistic* case we calculate an improvement of a factor  $\sim 1.6$ .

### 5.2 Analysis of the dark sirens

In Table 5, we report the median value and the 68% confidence level of the posterior distributions of the parameters of our *baseline* model for each SNR and for one, five and ten years of observations. These results are obtained by applying our pipeline to the *dark sirens*. As reported in Table 1, the number of events ranges from  $\sim 1 \times 10^4$  to  $\sim 5 \times 10^5$  and are located at a maximum redshift of  $\sim 6.9$  depending on the SNR and the total year of observations.

Since the redshift of the event is *a priori* unknown, we have to marginalize over it. Thus, adopting the probability distribution given in Eq. (10), we found that the Hubble constant may be detected with an accuracy of (at most of)  $\sigma_{H_0} \approx 0.04 \text{ km s}^{-1} \text{ Mpc}^{-1}$  using our *reference catalog*. This would represent an uncertainty at level

SNR	years	Realistic case			Optimistic case		
		$H_0$	$\Omega_{k,0}$	$\Omega_{\Lambda,0}$	$H_0$	$\Omega_{k,0}$	$\Omega_{\Lambda,0}$
9	1	$66.24^{+1.44}_{-1.46}$	$-0.04^{+0.40}_{-0.30}$	$0.67^{+0.24}_{-0.35}$	$66.96^{+1.05}_{-1.09}$	$0.15^{+0.34}_{-0.32}$	$0.50^{+0.25}_{-0.28}$
	5	$67.51^{+0.79}_{-0.83}$	$0.10^{+0.26}_{-0.21}$	$0.62^{+0.17}_{-0.19}$	$67.56^{+0.45}_{-0.47}$	$-0.02^{+0.11}_{-0.11}$	$0.70^{+0.08}_{-0.09}$
	10	$67.38^{+0.85}_{-0.84}$	$-0.08^{+0.17}_{-0.16}$	$0.71^{+0.13}_{-0.15}$	$67.47^{+0.39}_{-0.40}$	$-0.08^{+0.08}_{-0.09}$	$0.72^{+0.07}_{-0.07}$
12	1	$68.05^{+1.13}_{-1.10}$	$0.11^{+0.50}_{-0.30}$	$0.71^{+0.21}_{-0.33}$	$66.95^{+1.32}_{-1.17}$	$0.08^{+0.41}_{-0.32}$	$0.59^{+0.25}_{-0.31}$
	5	$67.45^{+0.99}_{-0.84}$	$-0.06^{+0.30}_{-0.24}$	$0.71^{+0.17}_{-0.24}$	$67.63^{+0.35}_{-0.36}$	$-0.07^{+0.16}_{-0.15}$	$0.70^{+0.11}_{-0.11}$
	10	$67.42^{+0.36}_{-0.34}$	$0.05^{+0.19}_{-0.17}$	$0.59^{+0.12}_{-0.12}$	$67.42^{+0.45}_{-0.44}$	$0.02^{+0.13}_{-0.13}$	$0.63^{+0.10}_{-0.10}$
15	1	$67.90^{+1.20}_{-1.33}$	$-0.09^{+0.48}_{-0.36}$	$0.70^{+0.22}_{-0.34}$	$67.84^{+0.51}_{-0.51}$	$-0.08^{+0.47}_{-0.34}$	$0.69^{+0.22}_{-0.29}$
	5	$67.33^{+0.93}_{-0.92}$	$0.26^{+0.36}_{-0.34}$	$0.49^{+0.24}_{-0.24}$	$68.13^{+0.61}_{-0.66}$	$-0.01^{+0.23}_{-0.19}$	$0.68^{+0.14}_{-0.15}$
	10	$68.10^{+0.68}_{-0.72}$	$-0.06^{+0.25}_{-0.20}$	$0.74^{+0.14}_{-0.18}$	$67.63^{+0.57}_{-0.62}$	$0.05^{+0.18}_{-0.17}$	$0.62^{+0.13}_{-0.13}$

**Table 3.** The median value and the 68% confidence level of the posterior distributions of the parameters of our *baseline* model for each SNR and for one, five and ten years of observations, as obtained from the MCMC analyses carried out on mock catalog collecting the GW events with a detected electromagnetic counterpart.

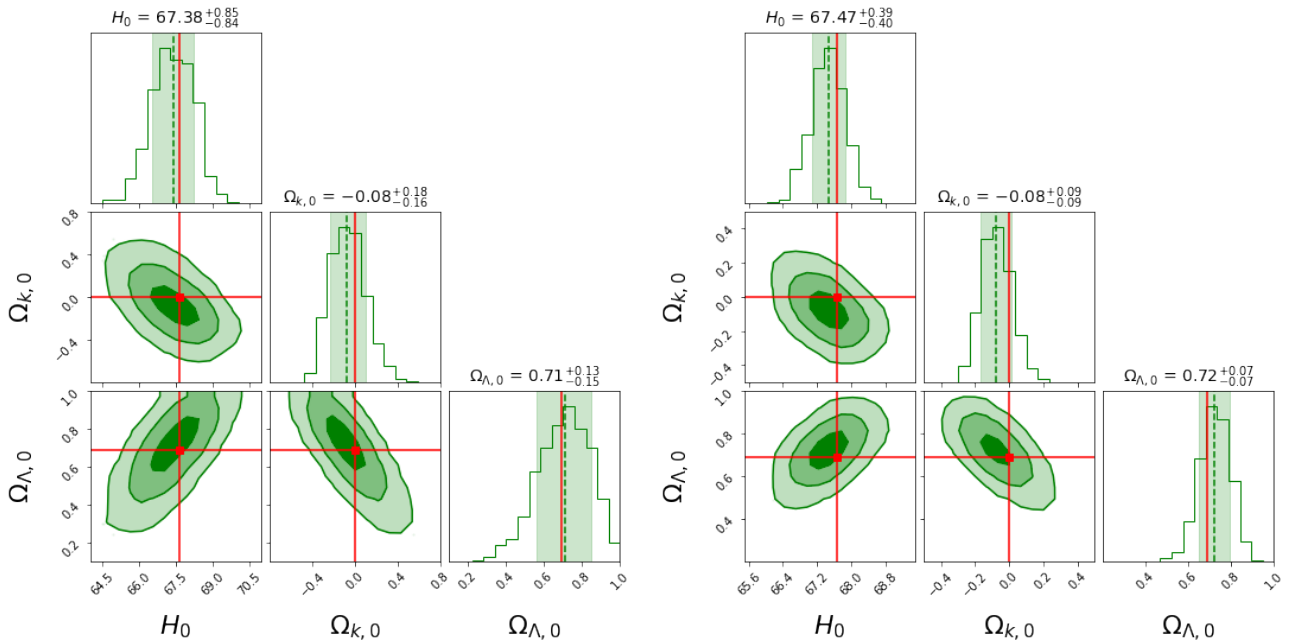


**Figure 4:** The figure illustrates the 68%, 95% and 99.7% of confidence level obtained from the posterior distribution of the parameters of our *baseline* model. The left and right panels show the results obtained from the *realistic* and *optimistic* analyses, respectively, carried out on the events detected after ten years of observations and using all the events with  $\text{SNR} > 9$ . The vertical red line in the histograms and a red point in the contour plot indicate the true values of the corresponding cosmological parameter. While, the vertical dashed line indicates the median value and the shaded band indicates the  $1\sigma$  confidence interval.

of  $\sim 0.06\%$ , about a factor 10 better than using only events with an electromagnetic counterpart. On the other hand, in the same analyses, the curvature parameter  $\Omega_{k,0}$  may be detected with an accuracy of  $\sigma_{\Omega_{k,0}} \approx 0.01$ . While, the cosmological constant density with an accuracy of  $\sigma_{\Omega_{\Lambda,0}} \approx 0.01$ , which represent an improvement of about a factor  $\sim 8$ . As a comparison Planck Collaboration constrains the Hubble constant with an accuracy of  $\sigma_{H_0} \approx 0.5 \text{ km s}^{-1} \text{ Mpc}^{-1}$ , and the cosmological constant density with an accuracy of  $\sigma_{\Omega_{\Lambda,0}} \approx 0.007$ . While, the curvature parameter is constrained with an accuracy of  $\sigma_{\Omega_{k,0}} \approx 0.02$  (Planck Collaboration et al. 2020b). In Figure 6, we show the contour plots corresponding to the 68%, 95% and 99.7% of confidence level obtained from the posterior distributions of the

parameters of our *baseline* model. Lines and colors follow the same design of Figure 4, and the true values of the cosmological parameters are again recovered within  $1\sigma$  but with an increased accuracy. For the sake of completeness, we report all the other contour plots in the Appendix C of SM.

The huge improvements show the full potential of the dark sirens. We can compare the results of Table 5 with those of Del Pozzo et al. (2017). On the cosmological densities, we confirm the order of magnitudes of the accuracy extrapolated by Del Pozzo et al. (2017). While on the Hubble constant, we note that the accuracy predicted by Del Pozzo et al. (2017) is much better than in our results analysis. One possible reason is that the SFR is assumed to be a constant

SNR	years	Realistic case			Optimistic case		
		$H_0$	$\Omega_{k,0}$	$\Omega_{\Lambda,0}$	$H_0$	$\Omega_{k,0}$	$\Omega_{\Lambda,0}$
9	1	$66.16^{+1.38}_{-1.56}$	$-0.07^{+0.47}_{-0.31}$	$0.66^{+0.25}_{-0.39}$	$66.92^{+1.03}_{-1.08}$	$0.16^{+0.41}_{-0.35}$	$0.48^{+0.29}_{-0.28}$
	5	$67.59^{+0.83}_{-0.85}$	$0.04^{+0.25}_{-0.20}$	$0.66^{+0.16}_{-0.19}$	$67.59^{+0.44}_{-0.46}$	$-0.04^{+0.12}_{-0.12}$	$0.71^{+0.08}_{-0.09}$
	10	$67.49^{+0.70}_{-0.87}$	$-0.11^{+0.16}_{-0.15}$	$0.74^{+0.12}_{-0.15}$	$67.46^{+0.41}_{-0.39}$	$-0.08^{+0.09}_{-0.09}$	$0.72^{+0.07}_{-0.08}$
12	1	$67.94^{+1.03}_{-1.16}$	$0.12^{+0.51}_{-0.33}$	$0.71^{+0.22}_{-0.34}$	$67.09^{+1.18}_{-1.36}$	$0.11^{+0.35}_{-0.33}$	$0.60^{+0.25}_{-0.29}$
	5	$67.61^{+0.87}_{-0.93}$	$-0.09^{+0.35}_{-0.23}$	$0.73^{+0.16}_{-0.26}$	$67.57^{+0.41}_{-0.37}$	$-0.06^{+0.16}_{-0.15}$	$0.68^{+0.15}_{-0.11}$
	10	$67.46^{+0.35}_{-0.34}$	$0.03^{+0.18}_{-0.15}$	$0.61^{+0.10}_{-0.12}$	$67.48^{+0.40}_{-0.47}$	$0.01^{+0.13}_{-0.13}$	$0.64^{+0.09}_{-0.10}$
15	1	$67.91^{+1.08}_{-1.30}$	$-0.11^{+0.50}_{-0.32}$	$0.73^{+0.20}_{-0.36}$	$67.97^{+0.42}_{-0.54}$	$-0.15^{+0.44}_{-0.29}$	$0.73^{+0.19}_{-0.28}$
	5	$67.26^{+0.91}_{-0.87}$	$0.28^{+0.35}_{-0.36}$	$0.49^{+0.25}_{-0.23}$	$67.97^{+0.65}_{-0.64}$	$0.06^{+0.22}_{-0.22}$	$0.65^{+0.15}_{-0.15}$
	10	$68.09^{+0.68}_{-0.70}$	$-0.08^{+0.22}_{-0.21}$	$0.74^{+0.15}_{-0.16}$	$67.75^{+0.55}_{-0.56}$	$0.01^{+0.18}_{-0.17}$	$0.65^{+0.12}_{-0.12}$

**Table 4.** The same as Table 3 but including the selection effects as discussed in Section 4.

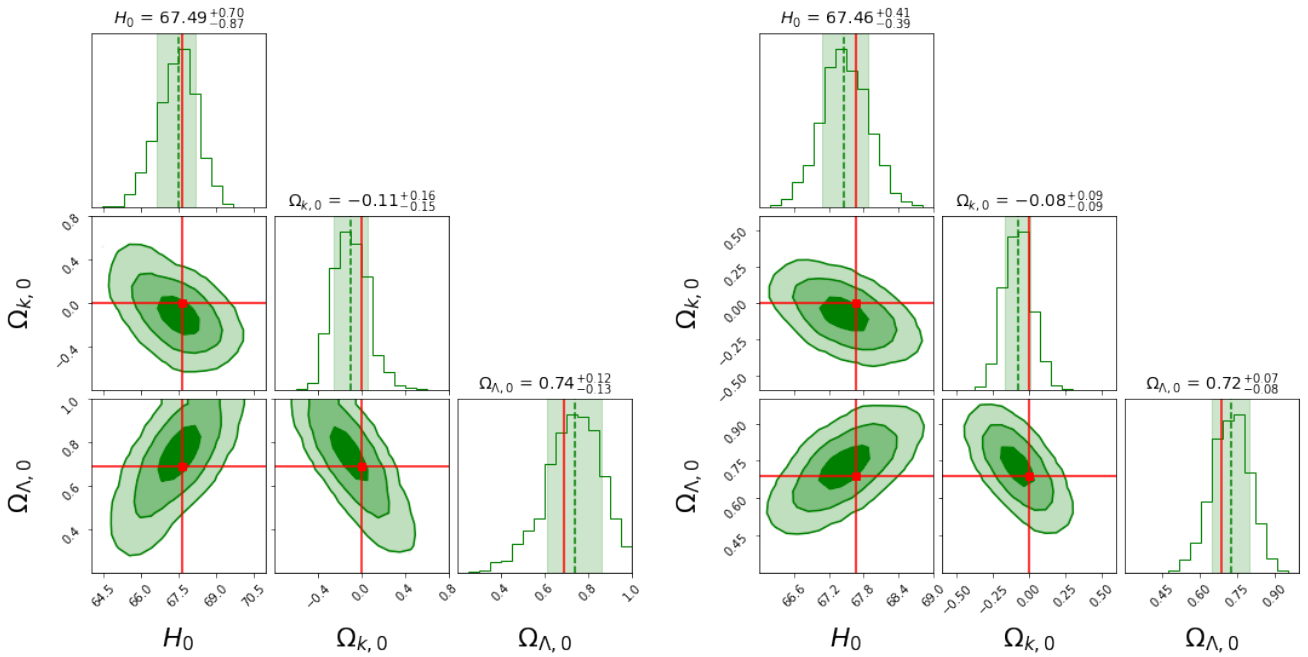


**Figure 5:** The same as Figure 4 but including the selection effects as discussed in Section 4.

giving more events at low redshift where the model is more sensitive to the value of the Hubble constant.

Our results for the *reference catalog* show an improvements of a factor of  $\sim 75$  and  $\sim 42$  in the accuracy on the Hubble constant with respect to the best constraints of Akarsu et al. (2021) and Di Valentino et al. (2021b), respectively. On the other hand, we improve a factor of  $\sim 16$  in the accuracy on the curvature parameter with respect to the best constraint of Akarsu et al. (2021), while we are comparable with the analysis of Di Valentino et al. (2021b).

Additionally, we also repeat the analysis adopting, to marginalize over the redshift, a Gaussian prior distribution centered on the *fiducial* redshift as it was obtained from the measurements of the tidal effects in BNS (Messenger & Read 2012; Jiang & Yagi 2021). As expected, even having partial information on the redshift with a statistical error of about 10%, which depends on neutron stars equation of state, the final results improve a factor 1.4 in the Hubble constant,  $\sigma_{H_0} \approx 0.03$

$\text{km s}^{-1} \text{Mpc}^{-1}$ , and a factor 2.5 in the curvature parameter,  $\sigma_{\Omega_{k,0}} \approx 0.004$ , and in the cosmological constant density,  $\sigma_{\Omega_{\Lambda,0}} \approx 0.004$ .

### 5.3 Impact of other star formation rates and the time delay distribution

Our *baseline* model adopts the *Vangioni model* for the SFR and the *power law* form of the time delay distribution. Here, we show that making other choices leads to similar constraints on the cosmological parameters. We consider three different models: **Model 1** based on the *Vangioni model* for the SFR and the *exponential distribution* of the time delay distribution; **Model 2** based on the *Madau - Dickison model* for the SFR and the *power law* form of the time delay distribution; **Model 3** based on the *Madau - Dickison model* for the SFR and the *exponential distribution* of the time delay distribution. For each model we repeat the analysis with  $\text{SNR} > 9$  and an observational pe-

Dark Sirens				
SNR	years	$H_0$	$\Omega_{k,0}$	$\Omega_{\Lambda,0}$
9	1	$67.70^{+0.13}_{-0.12}$	$0.00^{+0.02}_{-0.02}$	$0.67^{+0.02}_{-0.02}$
	5	$67.63^{+0.05}_{-0.05}$	$0.01^{+0.01}_{-0.01}$	$0.69^{+0.01}_{-0.01}$
	10	$67.68^{+0.04}_{-0.04}$	$0.00^{+0.01}_{-0.01}$	$0.69^{+0.01}_{-0.01}$
12	1	$67.56^{+0.21}_{-0.38}$	$-0.02^{+0.04}_{-0.03}$	$0.70^{+0.03}_{-0.03}$
	5	$67.62^{+0.06}_{-0.06}$	$0.01^{+0.01}_{-0.02}$	$0.74^{+0.08}_{-0.07}$
	10	$67.68^{+0.06}_{-0.05}$	$0.00^{+0.01}_{-0.01}$	$0.69^{+0.01}_{-0.01}$
15	1	$67.79^{+0.28}_{-0.41}$	$-0.07^{+0.07}_{-0.07}$	$0.70^{+0.03}_{-0.03}$
	5	$67.69^{+0.07}_{-0.07}$	$-0.00^{+0.03}_{-0.03}$	$0.68^{+0.02}_{-0.02}$
	10	$67.67^{+0.05}_{-0.06}$	$0.01^{+0.01}_{-0.01}$	$0.69^{+0.01}_{-0.01}$

**Table 5.** The same as Table 3 but for the dark sirens assuming known the redshift prior distribution.

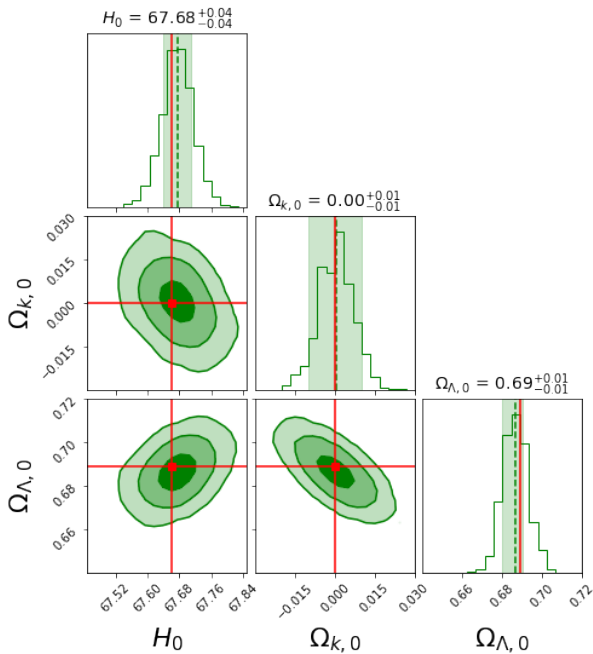


**Figure 6:** The same of Figure 4 but for the dark sirens assuming known the redshift prior distribution.

riod of ten years for both dark sirens and events with electromagnetic counterpart.

In Table 6, we report for each model the median values and the corresponding 68% of confidence level of the cosmological parameters. For both analyses the one considering only GW events with electromagnetic counterpart, and the other one using *dark sirens*. We found that the relative errors on the cosmological parameters are not affected by the particular choice of neither the SFR and the time delay distribution.

## 6 DISCUSSION AND CONCLUSIONS

We used mock catalogs of GW events from BNSs to forecast the precision down to which ET will be able to constrain the Hubble constant  $H_0$  and the curvature parameter  $\Omega_{k,0}$ . Although there were

GW + EM events				
MODEL	# events	$H_0$	$\Omega_{k,0}$	$\Omega_{\Lambda,0}$
<b>Baseline model</b>	332	$67.47^{+0.39}_{-0.40}$	$-0.08^{+0.08}_{-0.09}$	$0.72^{+0.07}_{-0.07}$
<b>Model 1</b>	603	$67.18^{+0.34}_{-0.32}$	$0.01^{+0.07}_{-0.07}$	$0.65^{+0.06}_{-0.06}$
<b>Model 2</b>	271	$67.48^{+0.30}_{-0.30}$	$-0.09^{+0.09}_{-0.10}$	$0.71^{+0.07}_{-0.07}$
<b>Model 3</b>	536	$67.20^{+0.27}_{-0.28}$	$0.01^{+0.08}_{-0.07}$	$0.65^{+0.05}_{-0.06}$

Dark Sirens				
MODEL	# events	$H_0$	$\Omega_{k,0}$	$\Omega_{\Lambda,0}$
<b>Baseline model</b>	521552	$67.68^{+0.04}_{-0.04}$	$0.00^{+0.01}_{-0.01}$	$0.69^{+0.01}_{-0.01}$
<b>Model 1</b>	1143212	$67.64^{+0.04}_{-0.04}$	$0.00^{+0.01}_{-0.01}$	$0.69^{+0.01}_{-0.01}$
<b>Model 2</b>	443560	$67.62^{+0.05}_{-0.05}$	$0.01^{+0.01}_{-0.01}$	$0.68^{+0.01}_{-0.01}$
<b>Model 3</b>	966659	$67.68^{+0.04}_{-0.04}$	$-0.01^{+0.01}_{-0.01}$	$0.68^{+0.01}_{-0.01}$

**Table 6.** The *baseline* model adopts the *Vangioni* model for the SFR and the *power law* form of the time delay distribution; **Model 1** is based on the *Vangioni* model for the SFR and the *exponential* distribution of the time delay distribution; **Model 2** is based on the *Madau - Dickison* model for the SFR and the *power law* form of the time delay distribution; **Model 3** is based on the *Madau - Dickison* model for the SFR and the *exponential* distribution of the time delay distribution.

other analyses carried out to measure the accuracy on the Hubble constant achievable with ET (Zhao et al. 2011; Cai & Yang 2017; Belgacem et al. 2019; Borhanian et al. 2020; Yang 2021; Leandro et al. 2022), these focused on a flat- $\Lambda$ CDM model. Therefore, the forecasts for a non-flat  $\Lambda$ CDM cosmology are currently missing. Hence, we built nine mock catalogs containing GW events for one, five, and ten years of observational runs, and for three different thresholds in SNR. Additionally, starting from each one of those nine mock catalogs, we extracted a mock catalog of GW events with associated (and detected) electromagnetic counterpart using THESEUS satellite. In Table 1 and 2, we report the number of events expected for each combination of SNR and observational run.

This is a proof-of-principle study and the accuracy reached in our analysis depends on the assumptions made to build the mock catalogs. Therefore, we report a list of such assumptions for sake of clearness:

- (i) we set the SFR to Eq. (14), and the time delay distribution to  $P(t_d) \propto t_d^{-1}$ . The model parameters of both are fixed;
- (ii) we set the value of  $R_m(z=0)$  to the one obtained by the LIGO/Virgo/Kagra collaboration The LIGO Scientific Collaboration et al. (2021c), and consequently, we assume that the NS masses range uniformly in the interval  $[1, 2.5] M_\odot$ ;
- (iii) we use the latest power spectral density for ET;
- (iv) we assume that the only contributions to luminosity distance error are given by (25);
- (v) in the modelling of the GW likelihood, we neglect of effect of GW detector sensitivity on the sky-position of the sources;
- (vi) we assume a Gaussian profile of the GRB jet, Eq. (30) and the distribution of GRB peak luminosity, Eq. (31);
- (vii) the number of combined events is strictly related to the features of THESEUS satellite.

Once mock catalogs have been compiled, we run our MCMC pipeline to forecast the accuracy down to which ET can recover the fiducial cosmological model used to build the mock catalog themselves. We run two sets of analyses: one that focused on catalogs of GW events with a detected electromagnetic counterpart, and another

that focused on the whole mock catalogs (including also events without a detected electromagnetic counterpart). In our best scenario, using the mock catalog that collects all the events detected after ten years of observations and using all the events with  $\text{SNR} > 9$ , we obtain that ET can constrain the cosmological parameters with an accuracy of  $\sigma_{H_0} \approx 0.40 \text{ km s}^{-1} \text{ Mpc}^{-1}$ ,  $\sigma_{\Omega_{k,0}} \approx 0.09$ , and  $\sigma_{\Omega_{\Lambda,0}} \approx 0.07$ , using only events with a detected electromagnetic counterpart. Our results show that ET may improve of  $\sim 76\%$  the accuracy on the Hubble constant with respect to the best scenario of Di Valentino et al. (2021b), and a factor of  $\sim 7.5$  with respect to Akarsu et al. (2021). When we consider all the GW events without the electromagnetic counterpart, *i.e.* *dark sirens*, we found that ET may constrain the cosmological parameters with an accuracy of  $\sigma_{H_0} \approx 0.04 \text{ km s}^{-1} \text{ Mpc}^{-1}$ ,  $\sigma_{\Omega_{k,0}} \approx 0.01$ , and  $\sigma_{\Omega_{\Lambda,0}} \approx 0.01$ . The improvements with respect to the previous analyses is due to the larger number of events under consideration, which mitigate not knowing the redshift *a priori*. Finally, we found that ET would improve of factor  $\sim 75$  and  $\sim 42$  the accuracy on the Hubble constant with respect to the best constraints of Akarsu et al. (2021) and Di Valentino et al. (2021b), respectively, and a factor of  $\sim 16$  in the accuracy on the curvature parameter with respect to the best constraint of Akarsu et al. (2021). These results show the huge potential of ET to strongly improve current constraints on the cosmological parameters of non-flat  $\Lambda$ CDM cosmology as they will be affected by different systematics compared to the analyses based on classical electromagnetic standard candles.

## ACKNOWLEDGMENTS

MC, DV, and SC acknowledge the support of Istituto Nazionale di Fisica Nucleare (INFN) iniziative specifiche MOONLIGHT2, QGSKY, and TEONGRAV. IDM acknowledges support from Ayuda IJCI2018-036198-I funded by MCIN/AEI/ 10.13039/501100011033 and: FSE “El FSE invierte en tu futuro” o “Financiado por la Unión Europea “NextGenerationEU”/PRTR. IDM is also supported by the projects PGC2018-096038-B-I00 and PID2021-122938NB-I00 funded by the Spanish “Ministerio de Ciencia e Innovación” and FEDER “A way of making Europe”, and by the project SA096P20 Junta de Castilla y León. DV also acknowledges the FCT project with ref. number PTDC/FIS-AST/0054/2021.

## Data Availability Statement

No new data were generated or analysed in support of this research.

## REFERENCES

Abbott B. P., et al., 2016a, *Phys. Rev. Lett.*, **116**, 061102  
 Abbott B. P., et al., 2016b, *Phys. Rev. Lett.*, **116**, 131103  
 Abbott B. P., et al., 2017a, *ApJ*, **848**, L12  
 Abbott B. P., et al., 2017b, *ApJ*, **848**, L13  
 Abdalla E., et al., 2022, arXiv e-prints, p. arXiv:2203.06142  
 Akarsu O., Di Valentino E., Kumar S., Ozyigit M., Sharma S., 2021, arXiv e-prints, p. arXiv:2112.07807  
 Alfradique V., Quartin M., Amendola L., Castro T., Toubiana A., 2022, arXiv e-prints, p. arXiv:2205.14034  
 Amati L., et al., 2018, *Advances in Space Research*, **62**, 191  
 Amati L., et al., 2021, *Experimental Astronomy*, **52**, 183  
 Amendola L., Kunz M., Saltas I. D., Sawicki I., 2018, *Phys. Rev. Lett.*, **120**, 131101  
 Baird E., Fairhurst S., Hannam M., Murphy P., 2013, *Phys. Rev. D*, **87**, 024035  
 Baker T., Bellini E., Ferreira P. G., Lagos M., Noller J., Sawicki I., 2017, *Phys. Rev. Lett.*, **119**, 251301

Band D., et al., 1993, *ApJ*, **413**, 281  
 Belczynski K., Perna R., Bulik T., Kalogera V., Ivanova N., Lamb D. Q., 2006, *ApJ*, **648**, 1110  
 Belgacem E., Dirian Y., Foffa S., Howell E. J., Maggiore M., Regimbau T., 2019, *J. Cosmology Astropart. Phys.*, **2019**, 015  
 Bera S., Rana D., More S., Bose S., 2020, *ApJ*, **902**, 79  
 Blanchet L., Iyer B. R., Will C. M., Wiseman A. G., 1996, *Classical and Quantum Gravity*, **13**, 575  
 Bonilla A., D’Agostino R., Nunes R. C., de Araujo J. C. N., 2020, *J. Cosmology Astropart. Phys.*, **2020**, 015  
 Borhanian S., Dhani A., Gupta A., Arun K. G., Sathyaprakash B. S., 2020, arXiv e-prints, p. arXiv:2007.02883  
 Cai R.-G., Yang T., 2017, *Phys. Rev. D*, **95**, 044024  
 Cai Y.-F., Li C., Saridakis E. N., Xue L.-Q., 2018, *Phys. Rev. D*, **97**, 103513  
 Capozziello S., De Laurentis M., 2012, *Annalen Phys.*, **524**, 545  
 Capozziello S., De Laurentis M., De Martino I., Formisano M., 2010, *Astroparticle Physics*, **33**, 190  
 Capozziello S., de Laurentis M., de Martino I., Formisano M., 2011, *Ap&SS*, **332**, 31  
 Capozziello S., Benetti M., Spallicci A. D. A. M., 2020, *Found. Phys.*, **50**, 893  
 Cen R., Ostriker J. P., 2000, *ApJ*, **538**, 83  
 Chan M. L., Messenger C., Heng I. S., Hendry M., 2018, *Phys. Rev. D*, **97**, 123014  
 Chatterjee D., Hegade K. R. A., Holder G., Holz D. E., Perkins S., Yagi K., Yunes N., 2021, *Phys. Rev. D*, **104**, 083528  
 Chen H.-Y., Fishbach M., Holz D. E., 2018, *Nature*, **562**, 545  
 Cigarrán Díaz C., Mukherjee S., 2022, *MNRAS*, **511**, 2782  
 Ciolfi R., et al., 2021, *Experimental Astronomy*, **52**, 245  
 Creminelli P., Vernizzi F., 2017, *Phys. Rev. Lett.*, **119**, 251302  
 Crisostomi M., Koyama K., 2018, *Phys. Rev. D*, **97**, 084004  
 Cutler C., Flanagan É. E., 1994, *Phys. Rev. D*, **49**, 2658  
 D’Agostino R., Nunes R. C., 2019, *Phys. Rev. D*, **100**, 044041  
 Dainotti M. G., De Simone B., Schiavone T., Montani G., Rinaldi E., Lambiase G., 2021, *ApJ*, **912**, 150  
 Dainotti M. G., De Simone B. D., Schiavone T., Montani G., Rinaldi E., Lambiase G., Bogdan M., Ugale S., 2022, *Galaxies*, **10**, 24  
 Dalal N., Holz D. E., Hughes S. A., Jain B., 2006, *Phys. Rev. D*, **74**, 063006  
 Del Pozzo W., 2012, *Phys. Rev. D*, **86**, 043011  
 Del Pozzo W., Li T. G. F., Messenger C., 2017, *Phys. Rev. D*, **95**, 043502  
 Di Valentino E., Melchiorri A., Silk J., 2020, *Nature Astronomy*, **4**, 196  
 Di Valentino E., et al., 2021a, *Classical and Quantum Gravity*, **38**, 153001  
 Di Valentino E., Melchiorri A., Silk J., 2021b, *ApJ*, **908**, L9  
 Ding X., Biesiada M., Zheng X., Liao K., Li Z., Zhu Z.-H., 2019, *J. Cosmology Astropart. Phys.*, **2019**, 033  
 Efstathiou G., Gratten S., 2020, *MNRAS*, **496**, L91  
 Ezquiaga J. M., Zumalacárregui M., 2017, *Phys. Rev. Lett.*, **119**, 251304  
 Finn L. S., 2001, *Phys. Rev. D*, **63**, 102001  
 Finn L. S., Chernoff D. F., 1993, *Phys. Rev. D*, **47**, 2198  
 Fixsen D. J., 2009, *ApJ*, **707**, 916  
 Foreman-Mackey D., Hogg D. W., Lang D., Goodman J., 2013, *Publications of the Astronomical Society of the Pacific*, **125**, 306  
 Ghirlanda G., et al., 2021, *Experimental Astronomy*, **52**, 277  
 Ghosh T., Biswas B., Bose S., 2022, arXiv e-prints, p. arXiv:2203.11756  
 Gray R., et al., 2020, *Phys. Rev. D*, **101**, 122001  
 Handley W., 2021, *Phys. Rev. D*, **103**, L041301  
 Hild S., et al., 2011, *Classical and Quantum Gravity*, **28**, 094013  
 Hirata C. M., Holz D. E., Cutler C., 2010, *Phys. Rev. D*, **81**, 124046  
 Hogg D. W., 1999, arXiv e-prints, pp astro-ph/9905116  
 Holz D. E., Hughes S. A., 2005, *ApJ*, **629**, 15  
 Howell E. J., Ackley K., Rowlinson A., Coward D., 2019, *MNRAS*, **485**, 1435  
 Jiang N., Yagi K., 2021, *Phys. Rev. D*, **103**, 124047  
 Jin S.-J., Wang L.-F., Wu P.-J., Zhang J.-F., Zhang X., 2021, *Phys. Rev. D*, **104**, 103507  
 Jin S.-J., Li T.-N., Zhang J.-F., Zhang X., 2022a, arXiv e-prints, p. arXiv:2202.11882  
 Jin S.-J., Zhu R.-Q., Wang L.-F., Li H.-L., Zhang J.-F., Zhang X., 2022b, arXiv e-prints, p. arXiv:2204.04689

- Kocsis B., Frei Z., Haiman Z., Menou K., 2006, *ApJ*, **637**, 27
- Kreisch C. D., Komatsu E., 2018, *J. Cosmology Astropart. Phys.*, **2018**, 030
- Lamb G. P., Kobayashi S., 2017, *MNRAS*, **472**, 4953
- Leandro H., Marra V., Sturani R., 2022, *Phys. Rev. D*, **105**, 023523
- Li Y., Heng I. S., Chan M. L., Messenger C., Fan X., 2022, *Phys. Rev. D*, **105**, 043010
- Lipunov V. M., Postnov K. A., Prokhorov M. E., Panchenko I. E., Jorgensen H. E., 1995, *ApJ*, **454**, 593
- Luongo O., Muccino M., 2022, arXiv e-prints, p. arXiv:2207.00440
- MacLeod C. L., Hogan C. J., 2008, *Phys. Rev. D*, **77**, 043512
- Madau P., Dickinson M., 2014, *ARA&A*, **52**, 415
- Maggiore M., 2007, *Gravitational Waves. Vol. 1: Theory and Experiments. Oxford Master Series in Physics*, Oxford University Press
- Maggiore M., et al., 2020, *J. Cosmology Astropart. Phys.*, **2020**, 050
- Mandel I., Farr W. M., Gair J. R., 2019, *MNRAS*, **486**, 1086
- Meacher D., et al., 2015, *Phys. Rev. D*, **92**, 063002
- Meacher D., Cannon K., Hanna C., Regimbau T., Sathyaprakash B. S., 2016, *Phys. Rev. D*, **93**, 024018
- Messenger C., Read J., 2012, *Phys. Rev. Lett.*, **108**, 091101
- Mészáros A., Řípa J., Ryde F., 2011, *A&A*, **529**, A55
- Mukherjee S., Wandelt B. D., Nissanke S. M., Silvestri A., 2021a, *Phys. Rev. D*, **103**, 043520
- Mukherjee S., Wandelt B. D., Silk J., 2021b, *MNRAS*, **502**, 1136
- Nava L., Ghirlanda G., Ghisellini G., Celotti A., 2011, *A&A*, **530**, A21
- Nissanke S., Holz D. E., Hughes S. A., Dalal N., Sievers J. L., 2010, *ApJ*, **725**, 496
- Nunes R. C., Vagnozzi S., 2021, *MNRAS*, **505**, 5427
- O’Shaughnessy R., Belczynski K., Kalogera V., 2008, *ApJ*, **675**, 566
- Padilla L. E., Tellez L. O., Escamilla L. A., Vazquez J. A., 2021, *Universe*, **7**, 213
- Park C.-G., Ratra B., 2020, *Phys. Rev. D*, **101**, 083508
- Philcox O. H. E., Ivanov M. M., Simonović M., Zaldarriaga M., 2020, *J. Cosmology Astropart. Phys.*, **2020**, 032
- Philcox O. H. E., Farren G. S., Sherwin B. D., Baxter E. J., Brout D. J., 2022, arXiv e-prints, p. arXiv:2204.02984
- Planck Collaboration et al., 2020a, *A&A*, **641**, A5
- Planck Collaboration et al., 2020b, *A&A*, **641**, A6
- Poisson E., Will C. M., 1995, *Phys. Rev. D*, **52**, 848
- Regimbau T., Hughes S. A., 2009, *Phys. Rev. D*, **79**, 062002
- Regimbau T., et al., 2012, *Phys. Rev. D*, **86**, 122001
- Regimbau T., Meacher D., Coughlin M., 2014, *Phys. Rev. D*, **89**, 084046
- Regimbau T., Siellez K., Meacher D., Gendre B., Boër M., 2015, *ApJ*, **799**, 69
- Regimbau T., Evans M., Christensen N., Katsavounidis E., Sathyaprakash B., Vitale S., 2017, *Phys. Rev. Lett.*, **118**, 151105
- Resmi L., et al., 2018, *ApJ*, **867**, 57
- Riess A. G., et al., 2021a, arXiv e-prints, p. arXiv:2112.04510
- Riess A. G., Casertano S., Yuan W., Bowers J. B., Macri L., Zinn J. C., Scolnic D., 2021b, *ApJ*, **908**, L6
- Rosati P., et al., 2021, *Experimental Astronomy*, **52**, 407
- Sakstein J., Jain B., 2017, *Phys. Rev. Lett.*, **119**, 251303
- Salucci P., et al., 2021, *Frontiers in Physics*, **8**, 579
- Sathyaprakash B. S., Schutz B. F., Van Den Broeck C., 2010, *Classical and Quantum Gravity*, **27**, 215006
- Schutz B. F., 1986, *Nature*, **323**, 310
- Schutz B. F., 2011, *Classical and Quantum Gravity*, **28**, 125023
- Shapiro C., Bacon D. J., Hendry M., Hoyle B., 2010, *MNRAS*, **404**, 858
- Speri L., Tamanini N., Caldwell R. R., Gair J. R., Wang B., 2021, *Phys. Rev. D*, **103**, 083526
- Stratta G., et al., 2018, *Advances in Space Research*, **62**, 662
- Tamanini N., Caprini C., Barausse E., Sesana A., Klein A., Petiteau A., 2016, *J. Cosmology Astropart. Phys.*, **2016**, 002
- The LIGO Scientific Collaboration et al., 2021a, arXiv e-prints, p. arXiv:2111.03604
- The LIGO Scientific Collaboration et al., 2021b, arXiv e-prints, p. arXiv:2111.03606
- The LIGO Scientific Collaboration et al., 2021c, arXiv e-prints, p. arXiv:2111.03634
- Tröster T., et al., 2021, *A&A*, **649**, A88
- Tutukov A. V., Yungelson L. R., 1994, *MNRAS*, **268**, 871
- Vagnozzi S., 2020, *Phys. Rev. D*, **102**, 023518
- Vagnozzi S., Loeb A., Moresco M., 2021, *ApJ*, **908**, 84
- Vangioni E., Olive K. A., Prestegard T., Silk J., Petitjean P., Mandic V., 2015, *MNRAS*, **447**, 2575
- Verde L., Treu T., Riess A. G., 2019, *Nature Astronomy*, **3**, 891
- Vitale S., Farr W. M., Ng K. K. Y., Rodriguez C. L., 2019, *ApJ*, **886**, L1
- Vitale S., Gerosa D., Farr W. M., Taylor S. R., 2020, arXiv e-prints, p. arXiv:2007.05579
- Wanderman D., Piran T., 2015, *MNRAS*, **448**, 3026
- Wang H., et al., 2017, *ApJ*, **851**, L18
- Wei J.-J., et al., 2017, *J. Cosmology Astropart. Phys.*, **2017**, 035
- Wong K. C., et al., 2020, *MNRAS*, **498**, 1420
- Yang T., 2021, *J. Cosmology Astropart. Phys.*, **2021**, 044
- Yang W., Vagnozzi S., Di Valentino E., Nunes R. C., Pan S., Mota D. F., 2019, *J. Cosmology Astropart. Phys.*, **2019**, 037
- Ye C., Fishbach M., 2021, *Phys. Rev. D*, **104**, 043507
- Yu J., et al., 2021, *ApJ*, **916**, 54
- Zhang J.-F., Zhang M., Jin S.-J., Qi J.-Z., Zhang X., 2019, *J. Cosmology Astropart. Phys.*, **2019**, 068
- Zhao W., Wen L., 2018, *Phys. Rev. D*, **97**, 064031
- Zhao W., van den Broeck C., Baskaran D., Li T. G. F., 2011, *Phys. Rev. D*, **83**, 023005
- de Freitas Pacheco J. A., Regimbau T., Vincent S., Spallicci A., 2006, *International Journal of Modern Physics D*, **15**, 235
- de Martino I., Chakrabarty S. S., Cesare V., Gallo A., Ostorero L., Diaferio A., 2020, *Universe*, **6**, 107

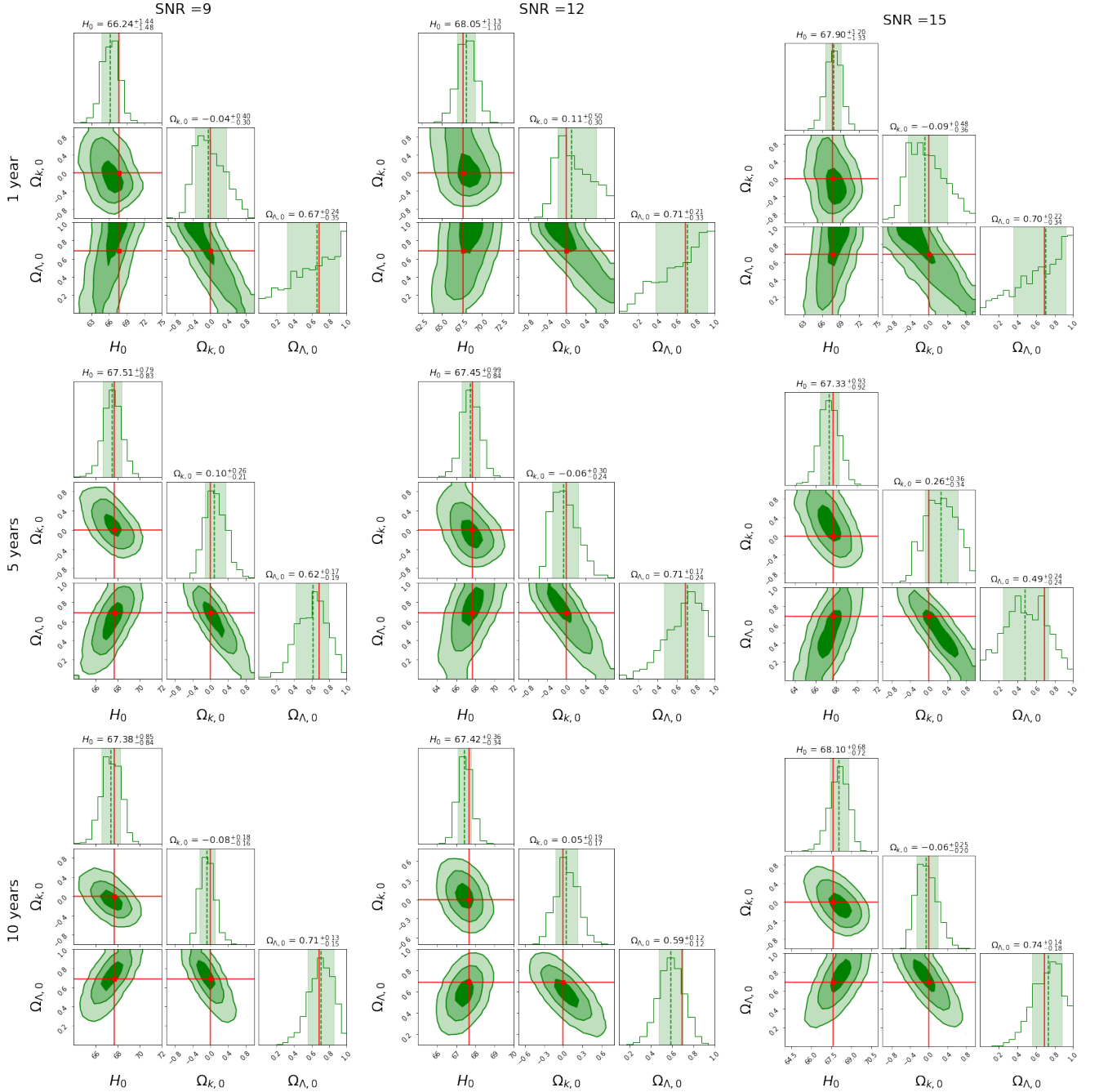
**APPENDIX A: CONTOURS PLOTS RELATIVE TO THE ANALYSIS OF GW EVENTS WITH A DETECTED ELECTROMAGNETIC COUNTERPART**


Figure A1: The figure illustrates the 68%, 95% and 99.7% of confidence level obtained from the posterior distribution of the parameters of our *baseline* model. The panels show the results obtained from the *realistic* analysis carried out on each catalog constructed. The vertical red line in the histograms and a red point in the contour plot indicates the true values of the corresponding cosmological parameter. While, the vertical dashed line indicates the median value and the shaded band indicates the  $1\sigma$  confidence interval.

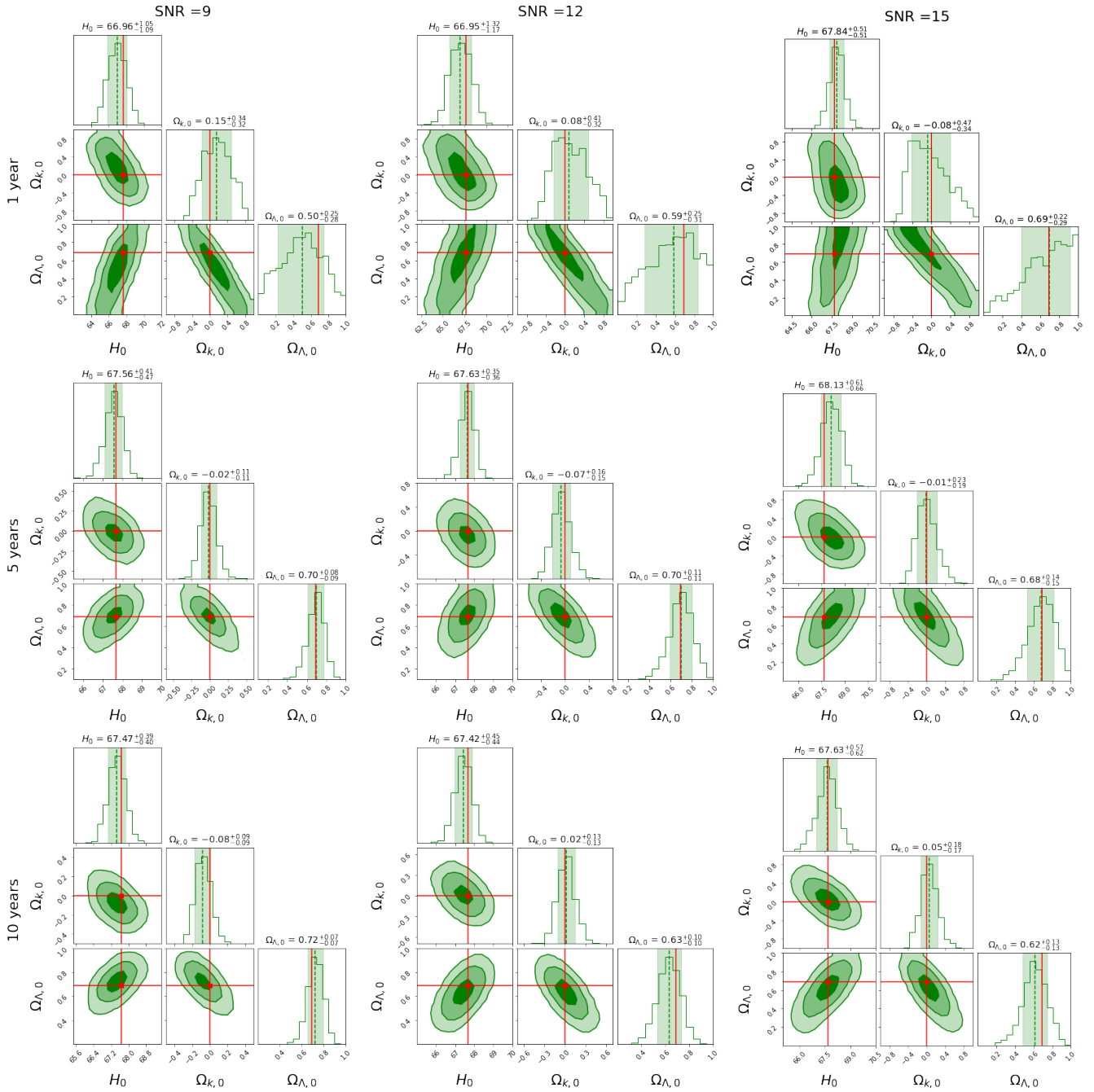


Figure A2: The same of Figure A1 but for the optimistic analysis.



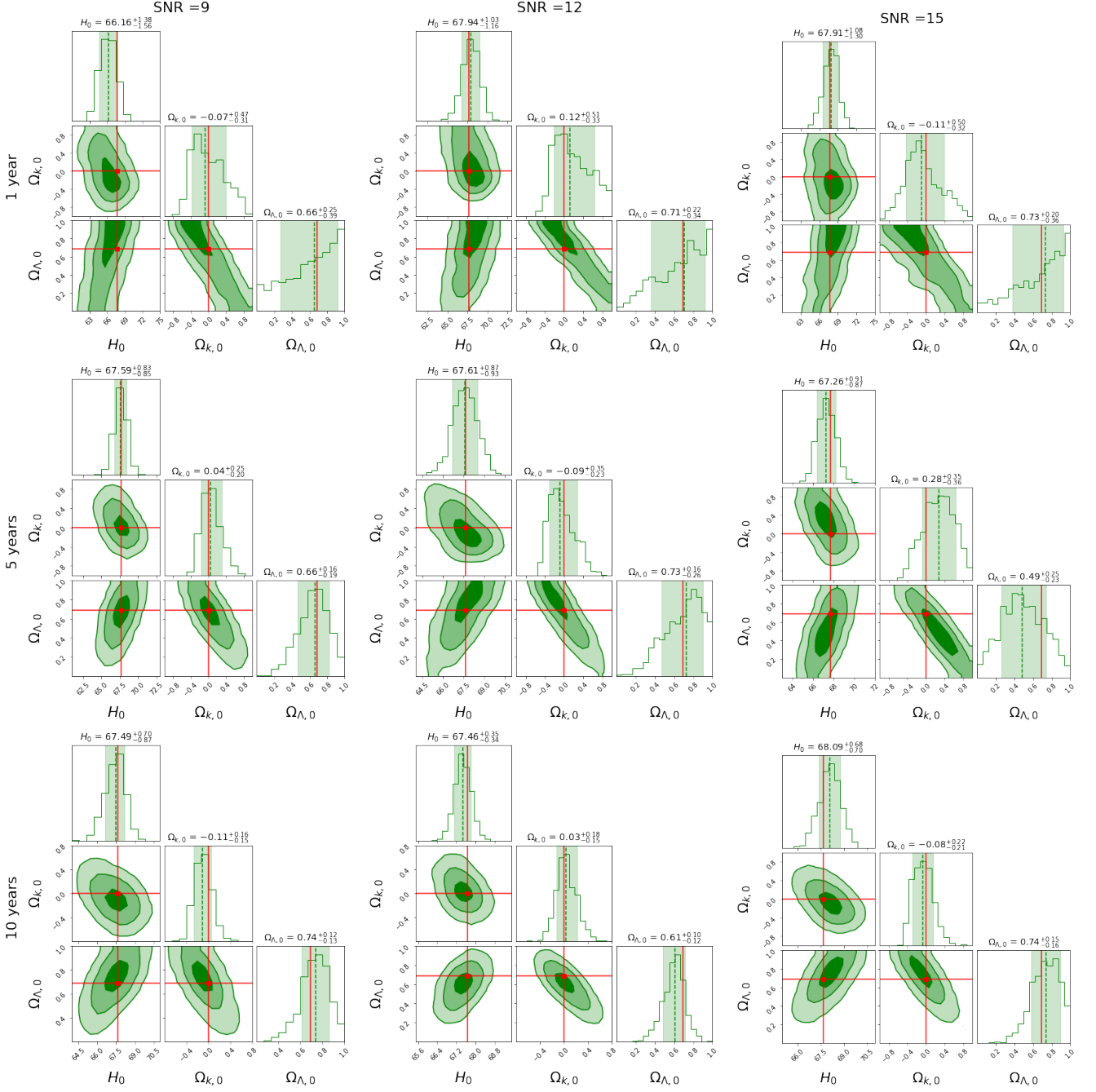
**APPENDIX B: CONTOURS PLOTS RELATIVE TO THE ANALYSIS INCLUDING THE SELECTION EFFECTS AND CARRIED OUT ON THE GW EVENTS WITH A DETECTED ELECTROMAGNETIC COUNTERPART**


Figure B1: The same of Figure A1 but including the selection effects as discussed in Section 4.

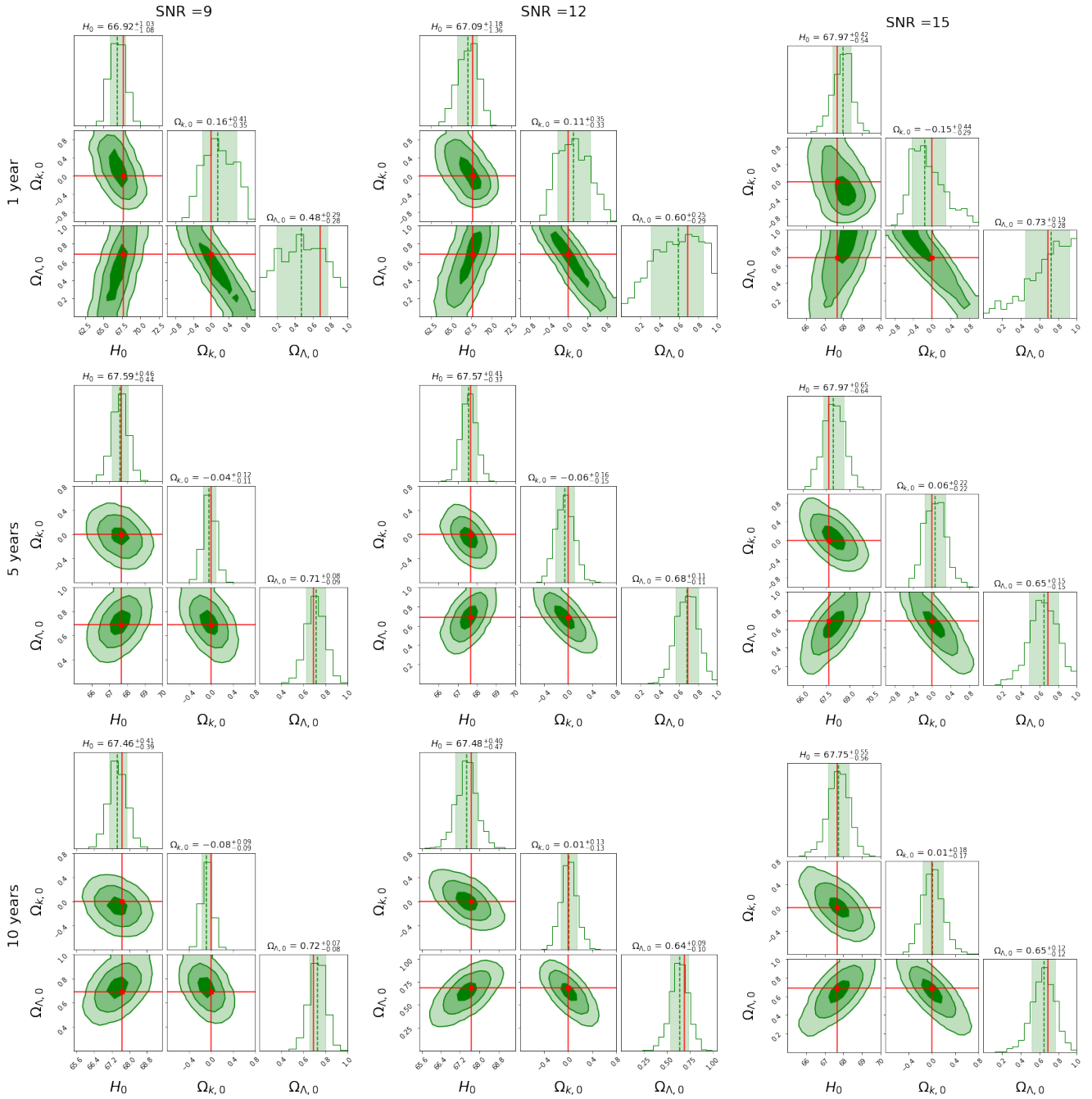


Figure B2: The same of Figure A1 but for the optimistic analysis and including the selection effects as discussed in Section 4.

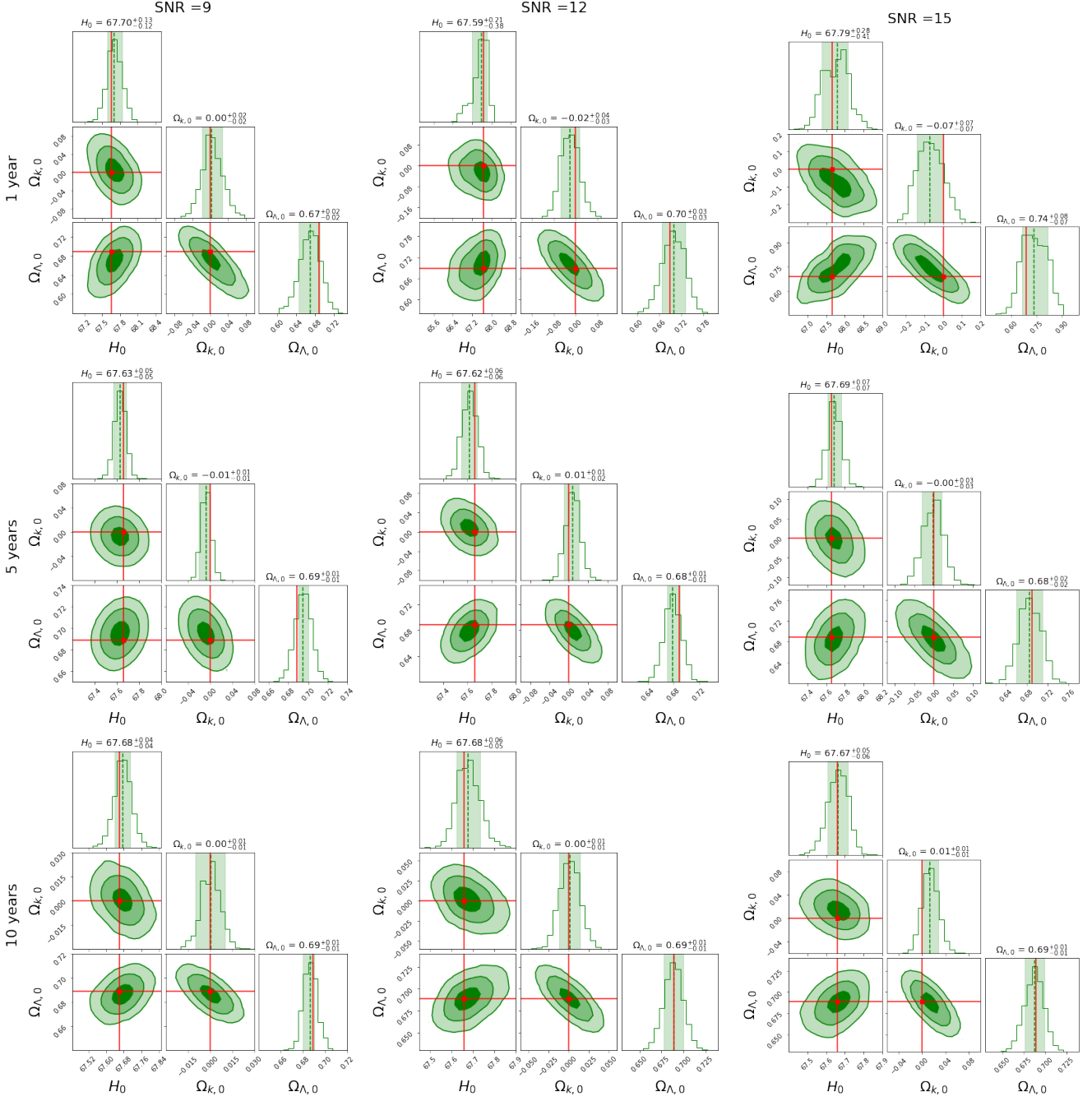
**APPENDIX C: CONTOURS PLOTS RELATIVE TO THE ANALYSIS ON THE DARK SIRENS ASSUMING A PRIOR REDSHIFT DISTRIBUTION**


Figure C1: The same of Figure A1 but for the dark sirens assuming known the redshift prior distribution

 This paper has been typeset from a  $\text{\TeX}/\text{\LaTeX}$  file prepared by the author.